

1 Revision 2

2 A method to estimate the pre-eruptive water content of basalts:
3 application to the Wudalianchi–Erkeshan–Keluo volcanic field,
4 Northeastern China

5
6 Yankun Di^{1,a}, Wei Tian^{1,*}, Mimi Chen¹, Zefeng Li^{2,b}, Zhuyin Chu³, Ju Liang¹

7
8 ¹School of Earth and Space Sciences, Peking University, Beijing 100871, China

9 ²School of Physics, Peking University, Beijing 100871, China

10 ³State Key Laboratory of Lithospheric Evolution, Institute of Geology and Geophysics,
11 Chinese Academy of Sciences, Beijing 100029, China

12
13 ^aPresent address: Research School of Earth Sciences, Australian National University,
14 Acton, ACT 2601, Australia

15 ^bPresent address: Research School of Astronomy & Astrophysics, Australian National
16 University, Weston Creek, ACT 2611, Australia

17 *Corresponding author, email: davidtian@pku.edu.cn

18

Abstract

19

Water plays an important role in the generation and evolution of volcanic systems.

20

However, the direct measurement of the pre-eruption water content of subaerial volcanic

21

rocks is difficult, because of the degassing during magma ascent. In this study, we

22

developed a method to calculate the pre-eruption water content of the basalts from the

23

Cenozoic Wudalianchi–Erkeshan–Keluo (WEK) potassic volcanic field, Northeastern

24

China, and investigated their mantle source. A water-insensitive clinopyroxene–melt

25

thermobarometer and a water-sensitive silica activity thermobarometer were applied to

26

these basalts. Two pressure–temperature (P – T) paths of the ascending magma were

27

calculated using these two independent thermobarometers, with a similar P – T slope but

28

clear offset. By adjusting the water content used in the calculation, the difference between

29

the two P – T paths was minimized, and the water content of the WEK melts was estimated

30

to be 4.5 ± 1.2 wt% at a pressure range of 10.1–13.5 kbar, corresponding to depths of 37–

31

47 km. Degassing modeling shows that during the magma ascent from below the Moho to

32

near the surface, CO_2 was predominantly degassed, while the melt H_2O content kept

33

stable. Significant H_2O degassing occurred until the magma ascended to 5–2 kbar. The

34

silica activity P – T estimates of the most primary WEK samples suggest that the magmas

35

were generated by the melting of convective mantle, which was probably facilitated by a

36

wet upwelling plume from the mantle transition zone. The high water content found in

37

the WEK basalts is similar to the recent reports on Phanerozoic intraplate large igneous

38

provinces (LIPs), and supports the presence of hydrated deep mantle reservoirs as one

39 possible source of the LIPs.

40

41 **Keywords:** water content, potassic basalt, degas, thermobarometer, Northeastern
42 China, Wudalianchi—Erkeshan—Keluo

43

44

Introduction

45 Water plays an important role in terrestrial and planetary magmatic processes
46 ([Hirschmann 2006](#); [O'Neill et al. 2007](#); [Wilson 2009](#); [Ni et al. 2016](#); [Peslier et al. 2017](#)).

47 In the source mantle, water controls the two most important factors constraining the
48 primary melt composition: the depth and degree of melting ([Katz et al. 2003](#); [Asimow
49 and Langmuir 2003](#)). During magma ascent, the exsolution of water can trigger
50 vesiculation and change the fluid dynamics of the volcanic system ([Gonnerman and
51 Manga 2007](#)). During the eruption, water can control the explosiveness and flow regime
52 ([Wilson 1980, 2009](#); [Kieffer 1995](#)). Thus, the water contents of magmas, especially the
53 water contents of primary melts, have long been investigated.

54 For magmas erupted on the deep seafloor, the primary water content can be
55 acquired by direct analysis of glass (e.g., [Michael 1995](#); [Dixon et al. 1997](#); [Hauri et al.
56 2002](#)). For subaerially erupted volcanic rocks, however, the estimation of the primary
57 water content is difficult due to the ubiquitous escape of volatiles during the eruption.
58 Primary melt inclusions are believed to be a good indicator of the pre-eruption water
59 content (e.g., [Hauri 2002](#); [Dixon and Clague 2001](#)); however, these inclusions are very

60 rare and easily altered by the interaction with the host minerals (Chen et al. 2011; Gaetani
61 et al. 2012). Another method is to measure the water content of clinopyroxene
62 phenocrysts and calculate the melt water content using a partitioning coefficient
63 $[K_D(\text{H}_2\text{O})^{\text{cpx-melt}}]$ (e.g., Wade et al. 2008; O’Leary et al. 2010), which, however, is not
64 applicable at all times as the water content of clinopyroxene decreases owing to the
65 diffusive re-equilibration with the melt during ascent-driven degassing (Cashman 2004;
66 Lloyd et al. 2016; Turner et al. 2017). Due to the diffusive water loss, both the melt
67 inclusion and phenocryst methods provide a minimal estimation of the pre-eruption water
68 content of the melt. Therefore, an ideal method of water content estimation for melts that
69 have experienced water exsolution is still required.

70 In this study, we develop a new method to determine the pre-eruption water
71 contents of melts by combining a water-insensitive and a water-sensitive
72 thermobarometer. The water-insensitive thermobarometer is based on the clinopyroxene–
73 melt equilibrium (Putirka et al. 2003) and has been widely applied for the pressure–
74 temperature (P – T) estimation of magmas with variable water contents (e.g., Putirka 1997,
75 2008; Putirka et al. 2009, 2012; Wang et al. 2012; Armienti et al. 2013). Another popular
76 thermobarometer, first established by Carmichael et al. (1970) and recalibrated by Lee et
77 al. (2009), is based on the Si activity in the olivine–melt–orthopyroxene equilibrium
78 system and is water-sensitive. Theoretically, these two thermobarometers should give
79 identical P – T estimates, i.e., they should plot onto a common P – T trajectory when
80 applied to the same volcanic field. Thus, we can obtain the water content of the melt by

81 fitting these two suites of P – T estimates into a common P – T trajectory. The water content
82 fitted by the thermobarometers can represent the actual quantity of water in the melt prior
83 to degassing.

84 Recently, the Cenozoic continental flood basalt (CFB) province in Central-East
85 Asia has been of interest to many researchers, owing to the arguments over whether it is
86 the product of dry melting of the hot upwelling mantle or of wet melting of the
87 transition-zone mantle hydrated by slab stagnation (Wang et al. 2015). The Wudalianchi–
88 Erkeshan–Keluo (WEK) potassic volcanic field, NE China, is the youngest representative
89 of this CFB province. Some researchers suggest that the WEK potassic basalts have a
90 relatively low water content (Chen et al. 2015), while others argue that the basalts were
91 derived from the melting of the highly hydrous transition-zone mantle (Kuritani et al.
92 2013). Here we apply the clinopyroxene–melt thermobarometer (Putirka et al. 2003) and
93 the Si activity thermobarometer (Lee et al. 2009) to the WEK volcanic rocks, with the
94 aims of estimating the water content of the WEK melts prior to degassing and
95 constraining their source mantle.

96

97 **Geological setting**

98 Cenozoic intraplate volcanic activity has occurred widely in Northeastern China
99 (Fig. 1). These eruptions began in the Late Cretaceous and have continued until recent
100 human history (Liu et al. 2001). Over 590 volcanic edifices and ~50,000 km² of surface
101 lava flows are distributed along the NNE/NE trending rift-graben systems (Zhou et al.

102 1988; Basu et al. 1991; Liu et al. 2001). Their compositions range from tholeiitic to
103 alkaline basalts, with more evolved trachybasalts, trachytes, and phonolites. These
104 volcanic rocks have been regarded either as a result of the replacement of the ancient
105 lithosphere by new, oceanic mantle (Xu et al. 2005, 2012; Tang et al. 2006) or related to
106 the stagnation of the Pacific slab in the mantle transition zone (Sakuyama et al. 2013;
107 Kuritani et al. 2011, 2013; Wang et al. 2015).

108 As one of the major alkaline volcanic rock fields in Northeastern China, the
109 Wudalianchi–Erkeshan–Keluo (WEK) volcanic field (Basu et al. 1991; #5 in Fig. 1) has
110 drawn special attention because of its highly potassic magma compositions (Zhang 1984;
111 Qiu 1991; Basu et al. 1991; Zhang et al. 1995, 1998; Zou et al. 2003; Chen et al. 2007;
112 Kuritani et al. 2013; Chu et al. 2013; Sun et al. 2014, 2015, 2017; Zhao et al. 2014a,
113 2014b; Liu et al. 2016; Tian et al. 2016; Wang et al. 2017). Recent studies also
114 demonstrated that this potassic volcanic field may extend to the adjacent Xiaogulihe site
115 (Shao et al. 2009; Sun et al. 2014). The WEK volcanoes erupted potassic magmas
116 including olivine leucitite, leucite basanite, and trachybasalt, at three episodes during
117 Miocene (9.6–7.0 Ma), middle Pleistocene (0.56–0.13 Ma), and recent human history
118 (1719–1721 A.D.; Zhang et al. 1995).

119 The WEK volcanic field contains substantial scoria cones with height/base
120 diameter ratios of ~0.2 (Zhao et al. 2014b). The lava flows are characterized by abundant
121 elongated vesicles as well as volcanic bombs on the flow surfaces (Fig. 2c). These field
122 characteristics indicate that the eruption styles of the WEK volcanoes were mainly

123 Strombolian type. Many mantle xenoliths are enclosed in the WEK basalts ([Zhang et al.](#)
124 [2000, 2011; Chen et al. 2007](#)).

125

126 **Sample description**

127 Twenty-six lava flow samples ([Table S1](#) in the Supplemental Materials) were
128 collected from the flow fields of Yaoquanshan volcano (acronym in [Table S1](#): YQ; same
129 as below), the proximal area of Laoheishan volcano (LHS), the distal area of Laoheishan
130 volcano (SC), Huoshaoshan volcano (HSS), the distal area of Jiaodebu volcano (GST),
131 Erkeshan volcano (KD), and Dayishan volcano (KL). We present major- and
132 trace-element results and Sr–Nd isotope data for all the 26 samples in [Tables S1](#) and [S2](#).
133 Eight samples were analyzed in this study; the remaining 18 were reported in [Chu et al.](#)
134 [\(2013\)](#). Mineral chemistry of clinopyroxene for six representative samples are listed in
135 [Table S3](#). The detailed methodology is described in [Appendix A](#) in the Supplemental
136 Materials.

137 Photographs of representative samples are provided in [Fig. 2](#). Based on mineral
138 mode compositions, the WEK potassic volcanic rocks are classified as olivine leucitites,
139 leucite basanites, and trachybasalts. The volcanic rocks are aphyric and glassy, containing
140 a small proportion of phenocrysts (<5%). These phenocrysts are less than 0.5 mm in
141 diameter and consist of olivine, clinopyroxene, and leucite. The presence of euhedral
142 olivine and clinopyroxene phenocrysts, together with melt inclusions, suggests a
143 magmatic rather than xenocrystic origin ([Chu et al. 2013](#)). Most clinopyroxene

144 phenocrysts do not show detectable zoning; some occasional oscillatory zoning (Fig. 2a)
145 observed indicates the normal pattern of crystal growth (Shore and Fowler 1996). The
146 embayment structure of olivine (Fig. 2d) indicates rapid decompression (Kuritani et al.
147 2013). The matrix mainly consists of quenched glass, olivine, clinopyroxene, K-feldspar,
148 and minor oxide minerals. Elongated bubbles, a typical gas-rich eruption feature,
149 ubiquitously occur in our samples (Figs. 2b, 2c). Mantle-derived peridotite xenoliths and
150 xenocrysts are present at each volcanic site.

151 On the total alkali–silica (TAS) diagram (Fig. S1), the WEK volcanic rock samples
152 plot in the areas of potassic phonotephrite, tephriphonolite, basaltic trachyandesite, and
153 trachyandesite. Although chemical classification shows that the WEK volcanic rocks are
154 not basalts, they have been consistently referred to as “potassic basalts” since Basu et al.
155 (1991). For consistency and simplicity, we adopt “potassic basalt” as a generalized name
156 for the WEK volcanic rocks.

157

158 **Thermobarometric methods**

159 **Clinopyroxene–melt thermobarometer**

160 The thermobarometer of Putirka et al. (2003) was applied to our WEK samples.
161 This thermobarometer was calibrated based on the jadeite–melt and jadeite–diopside +
162 hedenbergite exchange equilibrium thermodynamics, and the calibration dataset covers a
163 wide range of pressure (up to 35 kbar), temperature (850–1300 °C), and composition
164 (including Si-rich, alkali-rich, and hydrous melts). In our P – T calculations, the

165 clinopyroxene compositions were paired with their corresponding bulk-rock
166 compositions. For large clinopyroxene phenocrysts, multiple analytical spots were treated
167 individually. The standard estimate error (SEE) is 33 °C for temperature and 1.7 kbar for
168 pressure (Putirka et al. 2003).

169 There are several ways to test the equilibrium between clinopyroxene and melt (see
170 **Appendix B** in the Supplemental Materials for details); herein the Fe–Mg exchange test
171 was used before P – T calculation. The Fe–Mg exchange coefficient between
172 clinopyroxene and the equilibrated melt [$K_D(\text{Fe–Mg})^{\text{cpx–melt}} = (\text{Fe/Mg})^{\text{cpx}}/(\text{Fe/Mg})^{\text{melt}}$,
173 where Fe and Mg are in molar fraction] derived from 1,245 experimental observations
174 yields a roughly normal distribution ranging from 0.04 to 0.68, with a mean value of 0.28
175 and standard deviation (σ) of 0.08 (Putirka 2008). Using this criterion at 2σ level, 78 (out
176 of 122) equilibrated clinopyroxene–melt pairs with $K_D(\text{Fe–Mg})^{\text{cpx–melt}}$ between 0.12 and
177 0.44 were selected. All these clinopyroxene grains have $\text{Mg\#} > 75$ [$\text{Mg\#} =$
178 $100 \times \text{Mg}/(\text{Mg} + \text{Fe})$, where Fe and Mg are in molar fraction]. We plot the clinopyroxene
179 and bulk-rock Mg\# values in the Rhodes' diagram (Rhodes et al. 1979) (Fig. 3a) to
180 illustrate this equilibrium test. Nearly all the phenocrysts (including multi-spot analyses
181 on zoned phenocrysts) are in equilibrium with their host rocks. However, most
182 groundmass clinopyroxene grains exhibit disequilibrium features, suggesting that they
183 formed after significant magma crystallization, perhaps during the surface lava evolution.
184 Clinopyroxene grains that are not in equilibrium with their host rocks were excluded in
185 the P – T estimation.

186 The host bulk-rock composition of each clinopyroxene crystal was assumed as the
187 melt composition in our calculation, because the compositional evolution of the melt due
188 to crystallization is found to be negligible. The area analysis of thin-sections indicates
189 that phenocrysts (diameter ≤ 0.5 mm) occupy less than 5% of the thin-section area,
190 making their contribution to the modification of the melt composition insignificant. In
191 addition, the Mg# values of low-pressure clinopyroxene grains do not show a marked
192 decrease when compared to the higher-pressure ones (Fig. 3b). The groundmass
193 clinopyroxene grains have lower Mg# (Fig. 3a), but their crystallization occurred after the
194 crystallization of the high-Mg# phenocrysts. Therefore, the crystallization of groundmass
195 clinopyroxene grains could not have influenced the composition of the melt at deeper
196 depths. Finally, the melt-equilibrated clinopyroxene compositions simulated using the
197 models of Putirka (1999) at the P - T conditions obtained from thermobarometry are
198 identical to the measured clinopyroxene compositions within the prediction errors (Fig.
199 3c).

200

201 **Si activity thermobarometer**

202 The Si activity thermobarometer of Lee et al. (2009), which was calibrated based
203 on the thermodynamics of $\text{SiO}_2(\text{melt})$ - $\text{Mg}_2\text{SiO}_4(\text{olivine})$ - $\text{MgSiO}_3(\text{orthopyroxene})$
204 equilibrium, was applied to our samples. This thermobarometer was calibrated over a
205 wide range of pressure (up to 7 GPa), temperature (1100–1800 °C), and composition
206 (including Si-rich, alkali-rich, low-Mg#, and hydrous melts). The application of this

207 thermobarometer requires a melt water content input. Currently, no direct H₂O content
208 measurement for the WEK basalts is available, thus two H₂O contents were assumed in
209 our *P–T* calculation: 0.50 wt% (Chen et al. 2015) and 1.4 wt% (Kuritani et al. 2013). The
210 uncertainty is 2.0 kbar for pressure estimation and is 3% for temperature estimation (Lee
211 et al. 2009).

212 A major prerequisite for using the Si activity thermobarometer is that the melts are
213 in equilibrium with both olivine and orthopyroxene. The source mantle lithology of the
214 WEK basalts is dominated by peridotite rather than pyroxenite, based on the low Fe/Mn
215 ratios of olivine phenocrysts (Sun et al. 2014 and our unpublished data). In addition, the
216 mantle xenoliths recovered in the WEK lava consist of lherzolites and harzburgites
217 (Zhang et al. 2011). Therefore, the Si activity of the WEK melts tend to be consecutively
218 buffered by olivine and orthopyroxene during the mantle-level evolutions, such as partial
219 melting (polybaric or monobaric) and re-equilibration at shallower depths (Lee et al. 2009;
220 Plank and Forsyth 2016). Crustal assimilation and fractional crystallization, however, can
221 alter the equilibrated melt composition and cause underestimations of pressure and
222 temperature (Putirka et al. 2012; Plank and Forsyth 2016). The WEK basalts have not
223 experienced significant crustal assimilation, as evidenced by the rapid magma ascending
224 rates indicated by the occurrence of mantle xenoliths and significant ²³⁰Th excesses (Zou
225 et al. 2003), the uncontaminated mantle Os isotope and platinum group element
226 signatures (Chu et al. 2013; Sun et al. 2014), and the limited interactions between crust
227 xenoliths and the host lava (McGee et al. 2015). Fractional crystallization of olivine may

228 have occurred, but the degree is restricted to have negligible effects in generating the
229 observed magma composition variations (Zhang et al. 1995; Kuritani et al. 2013; Wang et
230 al. 2017). Thus, in principle, these basalts should have nearly mantle-equilibrated
231 signatures as exemplified by their high Mg#. We compiled 127 reliable WEK basalt
232 compositions with ferrous/ferric ratios from the literature (Qiu 1991; Zhang 1984). The
233 $\text{Fe}^{3+}/(\text{Fe}^{3+}+\text{Fe}^{2+})$ ratio shows a logarithmic normal distribution, with an expected value of
234 0.28. Using this $\text{Fe}^{3+}/(\text{Fe}^{3+}+\text{Fe}^{2+})$ ratio, we got better constrained Mg# values of 67–74
235 for our WEK samples. Combined with Tamura et al. (2000)'s composition-dependent
236 $K_D(\text{Fe-Mg})^{\text{ol-melt}}$, the olivine crystals in equilibrium with most WEK basalts (except
237 sample YQ4) have Fo values [Fo = $100 \times \text{Mg}/(\text{Mg}+\text{Fe})$, where Fe and Mg are in molar
238 fraction] ranging from 87 to 90, falling into the range of mantle xenolith olivine grains
239 discovered in this area (Zhang et al. 2000). Therefore, our WEK samples are likely to be
240 in equilibrium with the olivine and orthopyroxene in the proximal mantle, and the
241 crust-level evolutions should be negligible.

242 Another Si activity barometer, calibrated by Putirka (2008) based on the same
243 thermodynamic equilibrium but with a different Si activity expression and experimental
244 dataset (in similar P , T , melt composition, and H_2O ranges), was used to cross-check the
245 pressure estimates. With the same temperature inputs, the two independent barometers
246 yielded identical pressure estimates for our WEK basalts (Fig. 3d). This agreement
247 provides additional confidence for our P – T estimates.

248

249

Results

250 Clinopyroxene–melt thermobarometer

251 The P – T results of the clinopyroxene–melt thermobarometer are listed in [Table S3](#)
252 (in the Supplemental Materials) and plotted as blue circles in [Fig. 4a](#). The clinopyroxene
253 and the melt equilibrated at a pressure range of 0.8–13.5 kbar and a temperature range of
254 1051–1162 °C. The P – T results exhibit a linear trend of $P/\text{kbar} = -118.0 + 0.113 T/^\circ\text{C}$ (R^2
255 = 0.85).

256

257 Si activity thermobarometer

258 The P – T results of the Si activity thermobarometer are illustrated in [Fig. 4a](#). The
259 H₂O content of 0.50 wt% yields pressures between 8.8 and 15.5 kbar (corresponding to
260 depths of 33–54 km) and temperatures between 1129 and 1260 °C, and the H₂O content
261 of 1.4 wt% yields pressures between 9.1 and 15.6 kbar (corresponding to depths of 34–54
262 km) and temperatures between 1124 and 1247 °C. The P – T estimates from this
263 thermobarometer also exhibit linear trends, with a slope similar to that of the
264 clinopyroxene–melt thermobarometer. However, the intercepts with the T -axis of both Si
265 activity P – T arrays are different from that of the clinopyroxene–melt array.

266

267 Melt water content estimation

268 The plot of P – T results is generally divided into three pressure ranges ([Fig. 4a](#)): the
269 lower-pressure range determined only by the clinopyroxene–melt thermobarometer; the

270 higher-pressure range determined only by the Si activity thermobarometer; and the
271 overlapping pressure range in which both thermobarometers yielded P – T results. The
272 overlapping pressure range of two thermobarometers are from 8.8 to 13.5 kbar when the
273 0.50 wt% H₂O content is used, and from 9.1 to 13.5 kbar when the 1.4 wt% H₂O content
274 is used. At the overlapping pressure ranges, the temperatures estimated by the
275 clinopyroxene–melt thermobarometer tend to be systematically lower than those of the Si
276 activity thermobarometer.

277 There is only one real P – T path for the magmas, and both the thermobarometers
278 should reproduce this real P – T path. The clinopyroxene–melt thermobarometer (Putirka
279 et al. 2003) is independent of H₂O content, and hence the P – T path calculated by this
280 thermobarometer would represent the real P – T path within its SEE. However, the Si
281 activity thermobarometer of Lee et al. (2009) is water-sensitive. A higher H₂O content
282 used in the calculation can effectively increase the pressure but decrease the temperature,
283 as demonstrated by the contrast between the P – T paths calculated using the 1.4 wt% and
284 the 0.50 wt% H₂O content (Fig. 4a). When the actual melt H₂O content is used in the
285 calculation, the Si activity thermobarometer should generate a P – T path consistent with
286 the clinopyroxene–melt thermobarometer, i.e., both thermobarometers should generate
287 identical temperature estimates at the same pressure range. The observed offsets between
288 the P – T paths of the two thermobarometers in the overlapping pressure ranges (Fig. 4a)
289 therefore indicate that the H₂O contents used in the Si activity thermobarometer (0.50 wt%
290 and 1.4 wt%) may not represent the actual melt H₂O content. In contrast, the H₂O content

291 that minimizes the difference between the two P – T paths should be close to the actual
292 amount of water dissolved in the melt at the overlapping pressure range.

293 The temperature difference at the same pressure ($|\Delta T|$) between the P – T results of
294 the two thermobarometers varies with the H_2O content used in the calculation of the Lee
295 et al. (2009) thermobarometer (Table 1). We note that $|\Delta T|$ is minimized when the H_2O
296 content approaches ~5 wt%. Therefore, it is reasonable to suppose ~5 wt% as the actual
297 melt H_2O content in the overlapping pressure range of 10.3–13.5 kbar (Table 1). However,
298 this temperature difference is only a qualitative indicator based on the arbitrary judgment
299 of scattered data points. For most of the cases, due to the lack of a perfect match in
300 pressure, this arbitrary point-fitting method may not work well.

301 We instead propose to use a single parameter, “buffer overlapping area (BOA)”, to
302 evaluate the offset of the two P – T paths as a function of H_2O content. To construct a
303 buffer for a thermobarometer, the error ellipse of each P – T point estimated by this
304 thermobarometer was drawn on the P – T plot. The fields covered by these ellipses were
305 then outlined to form one (or more) closed shape(s), which is called a buffer. We
306 constructed buffers for the clinopyroxene–melt thermobarometer and the Si activity
307 thermobarometer (Fig. 4a) following this procedure. The overlapping “area” of the two
308 buffers in the P – T space, BOA, can be calculated when the H_2O content used in the Si
309 activity thermobarometer is known (details of the BOA calculation are given in Appendix
310 C in the Supplemental Materials). It is clear that, the smaller is the difference of the two
311 P – T paths, the larger is the BOA. Thus, when the BOA is maximized, the difference of

312 the two P – T paths is minimized. We calculated BOA values at H₂O contents from 0 wt%
313 to 9 wt% with increment of 0.1 wt%. The maximal BOA (BOA_{max}) was obtained for an
314 H₂O content of 4.5 wt%. In [Fig. 4b](#), we plot the BOA/BOA_{max} ratio against the melt
315 H₂O content used in the Si activity thermobarometer. This ratio reaches unity
316 (BOA/BOA_{max} = 1) when H₂O = 4.5 wt%, as expected. When the H₂O content is below
317 or above this value, BOA/BOA_{max} decreases gradually. Therefore, 4.5 wt% is taken as
318 our best estimate for the pre-eruptive WEK melt H₂O content at the overlapping pressure
319 range of 10.1–13.5 kbar (corresponding to depths of 37–47 km).

320 Quantifying the uncertainty of our estimate of the H₂O content, however, is not
321 explicit, because it has no direct error propagation relationship from the uncertainties of
322 the thermobarometers. Moreover, the systematic error in our estimation has not been
323 examined. Evaluation of the reliability and accuracy of our H₂O content estimation
324 method can be done with an experimentally-derived dataset of hydrous compositions. We
325 compiled twenty-one sets of experimental data with equilibrium phase assemblages of
326 melt + olivine + clinopyroxene + orthopyroxene ± other phases and $1 \leq \text{H}_2\text{O}^{\text{melt}} \leq 7$ wt%
327 from the Library of Experimental Phase Relations database (LEPR, [Hirshmann et al.](#)
328 [2008](#)) and summarize them in [Table 2](#). For each set of equilibrium phases, we estimated
329 the P – T conditions using the two thermobarometers, and then calculated BOAs with H₂O
330 content changing from 0 to 9 wt% with 0.1 wt% increment. In this case, a buffer is simply
331 an error ellipse instead of a closed shape formed by multiple ellipses. The melt H₂O
332 content was estimated as the H₂O content that maximizes the BOA, i.e., when the P – T

333 estimates of the two thermobarometers are the closest. Fig. 5a shows estimated versus
334 measured melt H₂O contents for the experimental equilibria. The H₂O content estimates
335 scatter near the 1:1 line, indicating no significant systematic error in our estimation. Our
336 method reproduces the experimental melt H₂O contents with standard estimate error
337 [standard estimate error (SEE) = $\sqrt{\sum(X_{\text{est}} - X_{\text{true}})^2/N}$, where X_{est} is the estimated value,
338 X_{true} is the true value, N is the number of data] of 1.2 wt%. Using the estimated H₂O
339 contents, the Si activity thermobarometer also reproduces the experimental P - T
340 conditions (Fig. 5b and 5c), confirming the inter-consistency of the models. Therefore,
341 we take the SEE of 1.2 wt% as an indicative uncertainty for our H₂O content estimate of
342 the WEK melts. This SEE may be further justified with larger testing datasets, and be
343 improved with better calibrations of thermobarometers.

344 The saturation temperature of clinopyroxene is controlled by the melt H₂O content
345 at a given pressure. All the WEK basalts are nearly aphyric with trace amount (<5 % area
346 in thin section) of clinopyroxene microphenocrysts, suggesting that the clinopyroxene
347 grains had crystallized when the magma temperatures were close to the clinopyroxene
348 saturation temperatures. By using the equation (34) of Putirka (2008), we calculated the
349 clinopyroxene saturation surfaces of a typical WEK potassic basalt sample, HSS5, at
350 different H₂O contents. The P - T path of the WEK magmas is roughly parallel to the
351 clinopyroxene saturation surfaces. At >5 kbar, nearly all the clinopyroxene-melt P - T
352 estimates are located between the clinopyroxene saturation surfaces with 4 and 5 wt%
353 H₂O (Fig. 4a). Such high H₂O contents are notably consistent with our estimate acquired

354 from the dual-thermobarometer method. This result also indicates that, nearly no decrease
355 of the melt H₂O content occurred during the magma decompression from 13.5 to 5 kbar.

356

357

Discussion

358 Elevated dT/dP of the magma and H₂O–CO₂ degassing

359 The linear regression of the P – T array of the WEK magma yielded a dT/dP value
360 of 8.8 °C/kbar (Fig. 4a). However, a basaltic magma isentropically (i.e., reversibly and
361 adiabatically) ascending through the lithosphere follows a P – T trajectory with $(\partial T/\partial P)_S \approx$
362 3.3 °C/kbar [or $(\partial T/\partial z)_S \approx 1.0$ °C/km, McKenzie and Bickle 1988; $(\partial T/\partial P)_S$: dT/dP when
363 the entropy is constant; $(\partial T/\partial z)_S$: dT/dz when the entropy is constant]. When the magma
364 ascends adiabatically but irreversibly (e.g., rapid ascending process), the $(\partial T/\partial P)_{Q,ir}$ value
365 [$(\partial T/\partial P)_{Q,ir}$: dT/dP when the heat is zero and the process is irreversible] decreases owing
366 to the generation of entropy (Ganguly 2008; Armienti et al. 2013). The isentropical
367 decompression slope $(\partial T/\partial P)_S$ is controlled by the thermal expansion coefficient (α),
368 specific heat capacity (c_p), and density (ρ) of the system (McKenzie and Bickle 1988).
369 Using the α , c_p , and ρ data listed in Table 3, our calculated $(\partial T/\partial P)_S$ for the volatile-free
370 HSS5 melt is 2.5 °C/kbar, close to the recommended value for basaltic melt (McKenzie
371 and Bickle 1988) but far lower than the regressed dT/dP value of 8.8 °C/kbar.

372 The heat loss through magma–wall rock interaction during the magma ascending
373 can increase the dT/dP value. However, the exceptionally hot eruption temperature
374 (~1250 °C) of the WEK magmas estimated by Kuritani et al. (2013) and the rapid ascent

375 constrained by significant ^{230}Th excesses (Zou et al. 2003) are consistent with extensive
376 magma–wall rock thermal interaction being unlikely. An alternative explanation of this
377 high dT/dP is the exsolution of volatiles, such as H_2O and CO_2 . Significant expansion of
378 fluid during adiabatic decompression can facilitate the cooling of the magma system,
379 leading to a high dT/dP value. As shown in Table 3, to produce such a high adiabatic
380 dT/dP value of $8.8\text{ }^\circ\text{C/kbar}$, the existence of fluid with high α and low ρ is required for
381 the WEK magma system.

382 The existence of a fluid phase indicates that the magma ascent is accompanied by
383 degassing. The pressure of volatile saturation depends on the contents of major volatile
384 species in the melt, i.e., H_2O and CO_2 . We have no direct constraint on the volatile
385 saturation pressure of the WEK magmas, because the melt CO_2 contents are unknown.
386 However, the ubiquitous occurrence of mantle xenoliths in the lava (Zhang et al. 2000)
387 strongly implies that the WEK magmas started degassing at mantle depths, as the
388 entrapment of xenoliths and the high magma transport rate essential for preserving the
389 xenoliths (10^{-1} to several m/s, Spera 1984) require rapid brittle failure (i.e., explosion) of
390 the mantle wall rock, which is most likely triggered by the formation of bubbles (Lensky
391 et al. 2006). Therefore, we assume that the melt dissolving 4.5 wt% H_2O is
392 volatile-saturated at 13.5 kbar and 1438 K (the deepest point on the clinopyroxene–melt
393 P – T array). At this state, the melt CO_2 content is predicted to be 2.0 wt% using the
394 solubility model of Duan (2014). If the pre-degassing melt CO_2 content was lower (or
395 higher) than 2.0 wt%, the degassing would start from a lower (or higher) pressure. As

396 shown in Fig. 6, the H₂O–CO₂ degassing along the *P–T* path of the WEK magmas in both
397 closed and open systems were simulated using the model of Duan (2014). From the
398 degassing curves, CO₂ was substantially removed from the melt when the pressure drops
399 from 13.5 kbar to 5 kbar, while the loss of H₂O was insignificant. At *P* < 5 kbar, the
400 degassing behavior of H₂O is distinct between closed and open systems: the onset of H₂O
401 exsolution from the melt was earlier in the closed system but later in the open system
402 until ~2 kbar. It is clear that the melt H₂O content of the ascending magma stayed
403 unchanged during high pressure degassing, which is in good agreement with the
404 clinopyroxene saturation surface calculation results above (Fig. 4a).

405

406 **Constraints on the source mantle**

407 The most unique geochemical characteristics of the WEK basalts are their
408 EM1-like Sr–Nd–Hf isotopes, low $\delta^{26}\text{Mg}$ values, and extremely unradiogenic Pb isotopes
409 (Zhang et al. 1995; Chu et al. 2013; Sun et al. 2014, 2017; Wang et al. 2017). The
410 correlations of these features indicate a recycled, isotopically “enriched” component in
411 the source mantle. However, the interpretation of this enriched component, coupled with
412 the issue of the ultimate source of the WEK magmas, is being debated. Several competing
413 theories concerning this problem have been put forward: (1) potassium-rich
414 sub-continental lithospheric mantle (SCLM) metasomatized by melt/fluid from ancient
415 asthenosphere (Zhang et al. 1995, 1998, 2000; Zou et al. 2003), delaminated Precambrian
416 lower crust fragments (Chu et al. 2013), or ancient subducted oceanic crust (Sun et al.

417 [2014, 2015, 2017](#)); (2) sub-lithospheric (or transition zone) mantle metasomatized by (or
418 mixed with) sediment fluid from an ancient stagnant slab ([Kuritani et al. 2013](#)), carbonate
419 melt from the modern Pacific slab ([Tian et al. 2016](#)), or remnants of an ancient
420 carbonate-bearing slab upwelled from the mantle transition zone (MTZ) ([Wang et al.](#)
421 [2017](#)). These conflicting models cannot provide a clear prospect about the real magma
422 source, thus evidence external to geochemical data are needed to constrain the origin of
423 the WEK volcanic rocks.

424 The source of the magmas can be located by determining the depths of melt
425 generation and transportation. We calculated the pressures and temperatures for six
426 low-SiO₂ melts from [Zhang et al. \(1995\)](#) using the [Lee et al. \(2009\)](#) Si activity
427 thermobarometer. Compared to our WEK dataset, these complimentary samples have
428 higher MgO contents (up to 14.40 wt%) and equilibrium Fo values (up to 92.0), thus
429 representing the compositions of more primary melts. They plot on the extrapolation of
430 our regressed P – T path and extend to higher P and T ([Fig. 7a](#)), suggesting that the WEK
431 melts originated from a deeper mantle. The deepest melt–olivine–orthopyroxene
432 equilibria occurred at 80–110 km (translated from $P = 23$ – 33 kbar). These depths
433 coincide with the low-velocity asthenosphere underlying the 70–80 km thick
434 high-velocity lithosphere lid from seismological constraints (e.g., [Zheng et al. 2011](#); [Li et](#)
435 [al. 2012, 2013](#); [Guo et al. 2014](#)), thus clearly indicating that the parental WEK melts were
436 generated beneath the SCLM. These P – T estimates lie closely along a hydrous peridotite
437 solidus with $X_{\text{H}_2\text{O}}^{\text{bulk}} = 450$ ppm (calculated using the model of [Katz et al. 2003](#), with

438 $X_{\text{H}_2\text{O}}^{\text{melt}} = 4.5 \text{ wt}\%$ from our estimation and a partitioning coefficient of 0.01), implying
439 that the melts can be generated by small-degree wet melting at these depths. If CO_2 has
440 further lowered the peridotite solidus (e.g., [Dasgupta et al. 2007](#)), melting may begin at a
441 greater depth, and the observed melt–mantle equilibrium depths may reflect the ponding
442 of melts at the base of the lithosphere. The stalled melts may thermally and chemically
443 erode the overlying lithosphere and cause its degradation ([Plank and Forsyth 2016](#);
444 [Putirka et al. 2012](#)). Overall, our inferred melting depths support the geochemical models
445 with a sub-lithospheric mantle origin of the WEK magmas.

446 The melting of the sub-lithospheric mantle may be related to the mantle upwelling
447 initiated from the MTZ. Recent high-resolution mantle tomography studies have revealed
448 large-scale (deep to $\sim 400 \text{ km}$), vertically continuous low-velocity anomalies beneath
449 WEK and other NE China Cenozoic volcanos ([Wei et al. 2019](#); [Ma et al. 2018](#); [Zhao et al.](#)
450 [2009](#)). The nature of this deep mantle upwelling, however, is debated. The upwelling of
451 wet mantle materials from the MTZ ([Kuritani et al. 2011, 2013, 2019](#); [Zhao et al. 2009](#))
452 or a hot mantle plume through a hole at the edge of the stagnant Pacific slab ([Tang et al.](#)
453 [2014](#)) have both been proposed for the origin of the deep back-arc volcanisms in NE
454 China. To examine whether excess heat contributed to the mantle upwelling beneath
455 WEK, we calculated the mantle potential temperature (T_p) using the [Putirka \(2016\)](#) model.
456 The most primary WEK melt compositions passed all the essential equilibrium tests of
457 this model, and yielded an average T_p of $1372 \pm 30 \text{ }^\circ\text{C}$. This T_p is significantly lower than
458 those of the intraplate volcanic hotspots (e.g., Hawaii and Samoa $T_p = 1722 \text{ }^\circ\text{C}$, [Putirka et](#)

459 al. 2007; Emeishan $T_p = 1740\text{--}1810$ °C, Tao et al. 2015; Siberian Trap $T_p = 1600$ °C,
460 Sobolev et al. 2011), but is similar to the ambient upper mantle temperature represented
461 by the average mid-ocean ridge ($T_p = 1454 \pm 78$ °C, Putirka et al. 2007) and the T_p of wet
462 arc or back-arc mantle in subduction zones (e.g., Mariana arc and trough $T_p = 1350$ °C,
463 Kelly et al. 2010; Yamato Basin, Japan Sea $T_p = 1200\text{--}1320$ °C, Hirahara et al. 2015;
464 Changbaishan, NE China $T_p = 1314\text{--}1357$ °C, Kuritani et al. 2019). This low- T_p
465 characteristic suggests that the mantle upwelling beneath the WEK area is not an active
466 plume driven by thermal buoyancy, but rather, facilitated by fluids released from the
467 stagnated Pacific slab in the MTZ (Kuritani et al. 2019; Richard and Bercovici 2009;
468 Richard and Iwamori 2010). The “wet plumes” (Iwamori 1991, 1992) may carry water
469 and other fluids from the MTZ to the upper mantle, and lead to wet melting in the
470 asthenosphere (Fig. 7b). This volatile-rich mantle source is consistent with our inferred
471 high H₂O (and CO₂) contents of the WEK magmas.

472

473 **Comparison with Xiaogulihe volcanic rocks: implication of mantle H₂O** 474 **heterogeneity**

475 The WEK potassic basalts and the Pleistocene ultrapotassic volcanic rocks from
476 Xiaogulihe (Fig. 1) are closely related in petrogenesis, owing to their similar geochemical
477 features, including high K₂O contents (4–9 wt%), strong enrichment of incompatible
478 elements (Fig. S3) compared to other Cenozoic basalts in eastern China and ocean island
479 basalts, and EM1-like Sr–Nd–Hf isotopic signatures (Zhang et al. 1998; Sun et al. 2014;

480 [Wang et al. 2017](#)). The melt H₂O contents of the Xiaogulihe volcanic rocks have been
481 estimated to be 0.36–0.50 wt%, based on Fourier transform infrared spectrometry
482 analyses of H₂O contents in clinopyroxene phenocrysts ([Chen et al. 2015](#)). Our 4.5 ± 1.2
483 wt% H₂O content estimation of the WEK melts is markedly higher than that of the
484 Xiaogulihe melts. We propose two possible explanations for this difference: (1) the
485 clinopyroxene phenocrysts analyzed by [Chen et al. \(2015\)](#) crystallized after significant
486 degassing; (2) the difference in melt H₂O content was inherited from the heterogeneous
487 H₂O abundance in the source mantle.

488 Analyzing the H₂O content of clinopyroxene can be a reliable method to retrieve
489 the primary (i.e., pre-eruption) melt H₂O content (e.g., [Wade et al. 2008](#); [Xia et al. 2013](#)).
490 Application of this method, however, requires that: (1) clinopyroxene had crystallized
491 before significant H₂O degassing; and (2) clinopyroxene had not experienced
492 degassing-associated H diffusion. By showing the invariant H₂O contents along profiles
493 within clinopyroxene crystals, [Chen et al. \(2015\)](#) demonstrated that the requirement (2)
494 was attained, while the requirement (1) was not fully verified. If the clinopyroxene grains
495 had crystallized during/after magma degassing at shallow depths (e.g., $P < 5$ kbar), they
496 may record reduced melt H₂O contents. To test this possibility, we calculated
497 crystallization pressures for the clinopyroxene grains analyzed by [Chen et al.](#) using the
498 [Putirka et al. \(2003\)](#) thermobarometer, and plotted pressure against the corresponding
499 melt H₂O content in [Fig. 8](#). The H₂O content of the Xiaogulihe melts remains constantly
500 low (~0.3 wt%) as the magma decompressed from 10 kbar to 3 kbar, but shows a notable

501 rise at $P < 3$ kbar. Considering the high clinopyroxene crystallization pressures (up to 10
502 kbar), as well as the low and constant melt H₂O content during the magma ascending, it is
503 unlikely that degassing occurred prior to the earliest clinopyroxene crystallization.
504 Therefore, we confirm that the clinopyroxene phenocrysts analyzed by [Chen et al. \(2015\)](#)
505 crystallized from undegassed melts, and the low H₂O content signature of the Xiaogulihe
506 melts is primary. The absence of deep degassing of the Xiaogulihe magmas is also
507 evidenced by the absence of mantle xenoliths at this volcanic site ([Zhang et al. 1998](#)), as
508 the generation and transport of xenoliths is highly dependent on volatile exsolution and
509 bubble nucleation ([Lensky et al. 2006](#)). The enhancement of melt H₂O content at $P < 3$
510 kbar can be explained by substantial shallow-level isobaric crystallization under
511 H₂O-undersaturated condition ([Blundy and Cashman 2008](#)), which is supported by the
512 observed high crystallinity (~40%) in the Xiaogulihe volcanic rocks ([Shao et al. 2009](#)).

513 Alternatively, the difference in H₂O content between the Xiaogulihe and WEK
514 volcanic rocks can be explained by a heterogeneous distribution of H₂O in the source
515 mantle, considering the >200 km distance between the two volcanic sites. Although
516 similar in geochemistry, the Xiaogulihe volcanic rocks exhibit more extreme
517 characteristics compared to the WEK basalts, such as the “ultra-high” K₂O contents (up
518 to 9.29 wt%, cf. 6.09 wt% for WEK), more enriched large-ion lithophile elements, more
519 fractionated rare earth elements, less radiogenic Pb isotope compositions, and lower
520 ¹⁴³Nd/¹⁴⁴Nd and higher ⁸⁷Sr/⁸⁶Sr ratios ([Zhang et al. 1998](#); [Sun et al. 2014](#); [Wang et al.](#)
521 [2017](#)). These features indicate a lower melting degree and an isotopically more enriched

522 source. If the source mantle of the Xiaogulihe volcanic rocks is less hydrous than that of
523 the WEK basalts, it is reasonable for these rocks to have a lower mantle melting degree at
524 given T_p , and therefore higher K_2O and incompatible element concentrations than the
525 WEK basalts.

526 A regional-scale mantle H_2O heterogeneity in eastern China has been recently
527 revealed; from southeast (close to Pacific subduction zone) to northwest (away from
528 Pacific subduction zone), the source mantle H_2O contents of the eastern China Cenozoic
529 basalts tend to decrease from 4700 ppm to 150 ppm (Chen et al. 2017; Xia et al. 2019).
530 The geochemical characteristics of these basalts are also influenced by increasing
531 subduction-related fluid activities with decreasing distance to the Pacific plate boundary
532 (Zhao et al. 2019). This spatial variation of mantle and magma hydration can be most
533 easily understood as the time-integrated contributions of the wet upwelling fluxes arising
534 from the MTZ during the subduction and stagnation of the Pacific slab. The Xiaogulihe
535 volcano is among the westernmost volcanisms in eastern China, ~200 km farther away
536 from the Pacific trench than WEK, and located far beyond the western edge of the
537 present-day stagnant Pacific slab (Fig. 1). Therefore, the water content contrast between
538 the WEK and Xiaogulihe volcanic rocks is consistent with the regional-scale variation
539 trend. We infer that the source mantle of the WEK and Xiaogulihe potassic volcanic rocks
540 is heterogeneously hydrated, and the Xiaogulihe volcanic rocks were derived from a less
541 hydrous domain.

542

543

Implications

544 In most subaerially erupted volcanic rocks, H₂O dissolved in the melt at depths
545 escapes when the magma ascends to shallower depths and flows towards the surface.
546 Traditionally, melt inclusion analyses and direct measurements of nominally anhydrous
547 minerals (NAMs) can help to constrain the H₂O content of the melt before eruption.
548 However, melt inclusions that preserve primitive H₂O contents are not easy to find, and H
549 in nominally anhydrous minerals is also susceptible to diffusive loss. The method
550 reported in this paper provides a new approach to estimate the primary H₂O contents of
551 subaerially erupted volcanic rocks despite their having experienced extensive degassing
552 before eruption. This quantitative H₂O content estimation is useful especially when no
553 direct H₂O analysis is available.

554 The Wudalianchi–Erkeshan–Keluo magma is an intraplate magma, which has long
555 been believed to have originated by the dry melting of a lithospheric mantle source.
556 However, our estimation of water contents shows that the WEK magmas with ~4.5 wt%
557 H₂O have as much water as some arc magmas. This finding is similar to the recent reports
558 on Phanerozoic intraplate large igneous provinces (LIPs) ([Xia et al. 2016](#); [Liu et al. 2017](#);
559 [Ivanov et al. 2018](#)), and supports the presence of hydrated deep mantle reservoirs as the
560 sources of these LIPs.

561 Our method is not restricted to primary melt inclusions or primary NAMs, and
562 therefore, it may be also applicable to some evolved magmatic samples, such as the
563 Martian nakhlite ([e.g., Peslier et al. 2019](#)) and chassignite meteorites.

564

565

Acknowledgements

566 We thank Zhongbo Gao and Miaoyuan Lang for help on programing and statistics,
567 Ping Zhang for discussion on the local seismology, and Guiming Shu and Xiaoli Li for
568 help on EPMA analysis. We appreciate the thorough review and instructive comments
569 from Keith Putirka and an anonymous reviewer. We also thank Anne Peslier for editorial
570 handling. We are grateful to Durgalakshmi for a careful proofreading of the manuscript.
571 This research was financially supported by the National Natural Science Foundation of
572 China (grant number 41630205, 41273018), the “973” Project of China (grant
573 number 2013CB429801) and National Student’s Platform for Innovation and
574 Entrepreneurship Training Program of China (grant number 201511001041). YD thank
575 “Tan Siu Lin Overseas Exchange Endowment for Undergraduates” for providing
576 financial support for the trip and presentation of this research in the 2016 Goldschmidt
577 conference. The authors would like to thank Enago (www.enago.cn) for their professional
578 English language editing.

579

580

References cited

581 Armienti, P., Perinelli, C., and Putirka, K.D. (2013) A new model to estimate deep-level
582 magma ascent rates, with applications to Mt. Etna (Sicily, Italy). *Journal of*
583 *Petrology*, 54(4), 795-813.
584 Asimow, P.D., and Langmuir, C.H. (2003) The importance of water to oceanic mantle

- 585 melting regimes. *Nature*, 421(6925), 815-820.
- 586 Basu, A.R., Wang, J.W., Huang, W.K., Xie, G.H., and Tatsumoto, M. (1991) Major
587 element, REE, and Pb, Nd and Sr isotopic geochemistry of cenozoic
588 volcanic-rocks of eastern China - implications for their origin from
589 suboceanic-type mantle reservoirs. *Earth and Planetary Science Letters*, 105(1-3),
590 149-169.
- 591 Blundy, J., and Cashman, K. (2008) Petrologic reconstruction of magmatic system
592 variables and processes. In K.D. Putirka, and F.J. Tepley, Eds. *Minerals,
593 Inclusions and Volcanic Processes*, 69, p. 179-239.
- 594 Bottinga, Y., and Richet, P. (1981) High pressure and temperature equation of state and
595 calculation of the thermodynamic properties of gaseous carbon dioxide. *American
596 Journal of Science*, 281(5), 615-660.
- 597 Carmichael, I.S.E., Nicholls, J., and Smith, A.L. (1970) Silica activity in igneous rocks.
598 *American Mineralogist*, 55(1-2), 246-263.
- 599 Cashman, K.V. (2004) Volatile controls on magma ascent and eruption. In R.S.J. Sparks,
600 and C.J. Hawkesworth, Eds. *State of the Planet: Frontiers and Challenges in
601 Geophysics*, 150, p. 109-124.
- 602 Chen, Y., Zhang, Y.X., Graham, D., Su, S.G., and Deng, J.F. (2007) Geochemistry of
603 Cenozoic basalts and mantle xenoliths in Northeast China. *Lithos*, 96(1-2),
604 108-126.
- 605 Chen, Y., Provost, A., Schiano, P., and Cluzel, N. (2011) The rate of water loss from

- 606 olivine-hosted melt inclusions. *Contributions to Mineralogy and Petrology*, 162(3),
607 625-636.
- 608 Chen, H., Xia, Q.K., and Ingrin, J. (2015) Water content of the Xiaogulihe ultrapotassic
609 volcanic rocks, NE China: implications for the source of the potassium-rich
610 component. *Science Bulletin*, 60(16), 1468-1470.
- 611 Chen, H., Xia, Q.-K., Ingrin, J., Deloule, E., and Bi, Y. (2017) Heterogeneous source
612 components of intraplate basalts from NE China induced by the ongoing Pacific
613 slab subduction. *Earth and Planetary Science Letters*, 459, 208-220.
- 614 Chu, Z.Y., Harvey, J., Liu, C.Z., Guo, J.H., Wu, F.Y., Tian, W., Zhang, Y.L., and Yang,
615 Y.H. (2013) Source of highly potassic basalts in northeast China: Evidence from
616 Re-Os, Sr-Nd-Hf isotopes and PGE geochemistry. *Chemical Geology*, 357, 52-66.
- 617 Dasgupta, R., Hirschmann, M.M., and Smith, N.D. (2007) Partial melting experiments of
618 peridotite CO₂ at 3 GPa and genesis of alkalic ocean island basalts. *Journal of*
619 *Petrology*, 48(11), 2093-2124.
- 620 Dixon, J.E., and Clague, D.A. (2001) Volatiles in basaltic glasses from Loihi seamount,
621 Hawaii: Evidence for a relatively dry plume component. *Journal of Petrology*,
622 42(3), 627-654.
- 623 Dixon, J.E., Clague, D.A., Wallace, P., and Poreda, R. (1997) Volatiles in alkalic basalts
624 from the North Arch volcanic field, Hawaii: Extensive degassing of deep
625 submarine-erupted alkalic series lavas. *Journal of Petrology*, 38(7), 911-939.
- 626 Duan, X. (2014) A general model for predicting the solubility behavior of H₂O-CO₂ fluids

- 627 in silicate melts over a wide range of pressure, temperature and compositions.
628 *Geochimica et Cosmochimica Acta*, 125, 582-609.
- 629 Gaetani, G.A., and Grove, T.L. (1998) The influence of water on melting of mantle
630 peridotite. *Contributions to Mineralogy and Petrology*, 131(4), 323-346.
- 631 Gaetani, G.A., Kent, A.J.R., Grove, T.L., Hutcheon, I.D., and Stolper, E.M. (2003)
632 Mineral/melt partitioning of trace elements during hydrous peridotite partial
633 melting. *Contributions to Mineralogy and Petrology*, 145(4), 391-405.
- 634 Gaetani, G.A., O'Leary, J.A., Shimizu, N., Bucholz, C.E., and Newville, M. (2012) Rapid
635 reequilibration of H₂O and oxygen fugacity in olivine-hosted melt inclusions.
636 *Geology*, 40(10), 915-918.
- 637 Ganguly, J. (2008) *Thermodynamics in Earth and Planetary Sciences*. Springer-Verlag
638 Berlin Heidelberg, Berlin.
- 639 Gonnermann, H.M., and Manga, M. (2007) The fluid mechanics inside a volcano. *Annual*
640 *Review of Fluid Mechanics*, 39, 321-356.
- 641 Grove, T.L., Holbig, E.S., Barr, J.A., Till, C.B., and Krawczynski, M.J. (2013) Melts of
642 garnet lherzolite: experiments, models and comparison to melts of pyroxenite and
643 carbonated lherzolite. *Contributions to Mineralogy and Petrology*, 166(3),
644 887-910.
- 645 Guo, Z., Cao, Y., Wang, X., John Chen, Y., Ning, J., He, W., Tang, Y., and Feng, Y. (2014)
646 Crust and upper mantle structures beneath Northeast China from receiver function
647 studies. *Earthquake Science*, 27(3), 265-275.

- 648 Hauri, E. (2002) SIMS analysis of volatiles in silicate glasses, 2: isotopes and abundances
649 in Hawaiian melt inclusions. *Chemical Geology*, 183(1-4), 115-141.
- 650 Hauri, E., Wang, J.H., Dixon, J.E., King, P.L., Mandeville, C., and Newman, S. (2002)
651 SIMS analysis of volatiles in silicate glasses 1. Calibration, matrix effects and
652 comparisons with FTIR. *Chemical Geology*, 183(1-4), 99-114.
- 653 Hesse, M., and Grove, T.L. (2003) Absarokites from the western Mexican Volcanic Belt:
654 constraints on mantle wedge conditions. *Contributions to Mineralogy and*
655 *Petrology*, 146(1), 10-27.
- 656 Hirahara, Y., Kimura, J.I., Senda, R., Miyazaki, T., Kawabata, H., Takahashi, T., Chang,
657 Q., Vaglarov, B.S., Sato, T., and Kodaira, S. (2015) Geochemical variations in
658 Japan Sea back-arc basin basalts formed by high-temperature adiabatic melting of
659 mantle metasomatized by sediment subduction components. *Geochemistry*
660 *Geophysics Geosystems*, 16(5), 1324-1347.
- 661 Hirschmann, M.M. (2006) Water, melting, and the deep earth H₂O cycle. *Annual Review*
662 *of Earth and Planetary Sciences*, 34(1), 629-653.
- 663 Hirschmann, M.M., Ghiorso, M.S., Davis, F.A., Gordon, S.M., Mukherjee, S., Grove,
664 T.L., Krawczynski, M., Medard, E., and Till, C.B. (2008) Library of Experimental
665 Phase Relations (LEPR): A database and Web portal for experimental magmatic
666 phase equilibria data. *Geochemistry, Geophysics, Geosystems*, 9(3).
- 667 Ivanov, A.V., Mukasa, S.B., Kamenetsky, V.S., Ackerson, M., Demonterova, E.I.,
668 Pokrovsky, B.G., Vladykin, N.V., Kolesnichenko, M.V., Litasov, K.D., and

- 669 Zedgenizov, D.A. (2018) Volatile concentrations in olivine-hosted melt inclusions
670 from meimechite and melanephelinite lavas of the Siberian Traps Large Igneous
671 Province: Evidence for flux-related high-Ti, high-Mg magmatism. *Chemical*
672 *Geology*, 483, 442-462.
- 673 Iwamori, H. (1991) Zonal structure of Cenozoic basalts related to mantle upwelling in
674 Southwest Japan. *Journal of Geophysical Research-Solid Earth and Planets*,
675 96(B4), 6157-6170.
- 676 —. (1992) Degree of melting and source composition of cenozoic basalts in Southwest
677 Japan - evidence for mantle upwelling by flux melting. *Journal of Geophysical*
678 *Research-Solid Earth*, 97(B7), 10983-10995.
- 679 Katz, R.F., Spiegelman, M., and Langmuir, C.H. (2003) A new parameterization of
680 hydrous mantle melting. *Geochemistry Geophysics Geosystems*, 4, 19.
- 681 Kelemen, P.B., Joyce, D.B., Webster, J.D., and Holloway, J.R. (1990) Reaction between
682 ultramafic rock and fractionating basaltic magma .2. Experimental investigation
683 of reaction between olivine tholeiite and harzburgite at
684 1150-degrees-c-1050-degrees-c and 5 kb. *Journal of Petrology*, 31(1), 99-134.
- 685 Kelley, K.A., Plank, T., Newman, S., Stolper, E.M., Grove, T.L., Parman, S., and Hauri,
686 E.H. (2010) Mantle melting as a function of water content beneath the Mariana
687 Arc. *Journal of Petrology*, 51(8), 1711-1738.
- 688 Kieffer, S.W. (1995) Numerical-models of caldera-scale volcanic-eruptions on Earth,
689 Venus, and Mars. *Science*, 269(5229), 1385-1391.

- 690 Kuritani, T., Ohtani, E., and Kimura, J.I. (2011) Intensive hydration of the mantle
691 transition zone beneath China caused by ancient slab stagnation. *Nature*
692 *Geoscience*, 4(10), 713-716.
- 693 Kuritani, T., Kimura, J.I., Ohtani, E., Miyamoto, H., and Furuyama, K. (2013) Transition
694 zone origin of potassic basalts from Wudalianchi volcano, Northeast China.
695 *Lithos*, 156, 1-12.
- 696 Kuritani, T., Xia, Q.K., Kimura, J., Liu, J., Shimizu, K., Ushikubo, T., Zhao, D.P.,
697 Nakagawa, M., and Yoshimura, S. (2019) Buoyant hydrous mantle plume from
698 the mantle transition zone. *Scientific Reports*, 9.
- 699 Lee, C.T.A., Luffi, P., Plank, T., Dalton, H., and Leeman, W.P. (2009) Constraints on the
700 depths and temperatures of basaltic magma generation on Earth and other
701 terrestrial planets using new thermobarometers for mafic magmas. *Earth and*
702 *Planetary Science Letters*, 279(1-2), 20-33.
- 703 Lensky, N.G., Niebo, R.W., Holloway, J.R., Lyakhovskiy, V., and Navon, O. (2006)
704 Bubble nucleation as a trigger for xenolith entrapment in mantle melts. *Earth and*
705 *Planetary Science Letters*, 245(1-2), 278-288.
- 706 Leshner, C.E., and Spera, F.J. (2015) Thermodynamic and transport properties of silicate
707 melts and magma. In H. Sigurdsson, B. Houghton, S. McNutt, H. Rymer, and J.
708 Stix, Eds. *The Encyclopedia of Volcanoes (Second Edition)*, p. 113-141.
709 Academic Press, Amsterdam.
- 710 Li, Y.H., Wu, Q.J., Pan, J.T., and Sun, L. (2012) S-wave velocity structure of northeastern

- 711 China from joint inversion of Rayleigh wave phase and group velocities.
712 Geophysical Journal International, 190(1), 105-115.
- 713 Li, Y.H., Wu, Q.J., Pan, J.T., Zhang, F.X., and Yu, D.X. (2013) An upper-mantle S-wave
714 velocity model for East Asia from Rayleigh wave tomography. Earth and
715 Planetary Science Letters, 377, 367-377.
- 716 Liu, J.Q., Han, J.T., and Fyfe, W.S. (2001) Cenozoic episodic volcanism and continental
717 rifting in northeast China and possible link to Japan Sea development as revealed
718 from K-Ar geochronology. Tectonophysics, 339(3-4), 385-401.
- 719 Liu, J.Q., Chen, L.H., Zeng, G., Wang, X.J., Zhong, Y., and Yu, X. (2016) Lithospheric
720 thickness controlled compositional variations in potassic basalts of Northeast
721 China by melt-rock interactions. Geophysical Research Letters, 43(6), 2582-2589.
- 722 Liu, J., Xia, Q.K., Kuritani, T., Hanski, E., and Yu, H.R. (2017) Mantle hydration and the
723 role of water in the generation of large igneous provinces. Nature
724 Communications, 8.
- 725 Lloyd, A.S., Ferriss, E., Ruprecht, P., Hauri, E.H., Jicha, B.R., and Plank, T. (2016) An
726 assessment of clinopyroxene as a recorder of magmatic water and magma ascent
727 rate. Journal of Petrology, 57(10), 1865-1886.
- 728 Ma, J.C., Tian, Y., Liu, C., Zhao, D.P., Feng, X., and Zhu, H.X. (2018) P-wave
729 tomography of Northeast Asia: Constraints on the western Pacific plate
730 subduction and mantle dynamics. Physics of the Earth and Planetary Interiors, 274,
731 105-126.

- 732 McGee, L.E., McLeod, C., and Davidson, J.P. (2015) A spectrum of disequilibrium
733 melting preserved in lava-hosted, partially melted crustal xenoliths from
734 the Wudalianchi volcanic field, NE China. *Chemical Geology*, 417, 184-199.
- 735 McKenzie, D., and Bickle, M.J. (1988) The volume and composition of melt generated
736 by extension of the lithosphere. *Journal of Petrology*, 29(3), 625-679.
- 737 Michael, P. (1995) Regionally distinctive sources of depleted MORB - evidence from
738 trace-elements and H₂O. *Earth and Planetary Science Letters*, 131(3-4), 301-320.
- 739 Muntener, O., Kelemen, P.B., and Grove, T.L. (2001) The role of H₂O during
740 crystallization of primitive arc magmas under uppermost mantle conditions and
741 genesis of igneous pyroxenites: an experimental study. *Contributions to
742 Mineralogy and Petrology*, 141(6), 643-658.
- 743 Ni, H.W., Zhang, L., and Guo, X. (2016) Water and partial melting of Earth's mantle.
744 *Science China-Earth Sciences*, 59(4), 720-730.
- 745 O'Leary, J.A., Gaetani, G.A., and Hauri, E.H. (2010) The effect of tetrahedral Al³⁺ on the
746 partitioning of water between clinopyroxene and silicate melt. *Earth and Planetary
747 Science Letters*, 297(1-2), 111-120.
- 748 O'Neill, C., Jellinek, A.M., and Lenardic, A. (2007) Conditions for the onset of plate
749 tectonics on terrestrial planets and moons. *Earth and Planetary Science Letters*,
750 261(1-2), 20-32.
- 751 Peslier, A.H., Schönbacher, M., Busemann, H., and Karato, S.I. (2017) Water in the
752 Earth's interior: Distribution and origin. *Space Science Reviews*, 212(1-2),

- 753 743-810.
- 754 Peslier, A.H., Hervig, R., Yang, S., Humayun, M., Barnes, J.J., Irving, A.J., and Brandon,
755 A.D. (2019) Determination of the water content and D/H ratio of the martian
756 mantle by unraveling degassing and crystallization effects in nakhlites.
757 *Geochimica et Cosmochimica Acta*, in press.
- 758 Plank, T., and Forsyth, D.W. (2016) Thermal structure and melting conditions in the
759 mantle beneath the Basin and Range province from seismology and petrology.
760 *Geochemistry Geophysics Geosystems*, 17(4), 1312-1338.
- 761 Putirka, K. (1997) Magma transport at Hawaii: Inferences based on igneous
762 thermobarometry. *Geology*, 25(1), 69-72.
- 763 — (1999) Clinopyroxene plus liquid equilibria to 100 kbar and 2450 K. Contributions
764 to *Mineralogy and Petrology*, 135(2-3), 151-163.
- 765 — (2008) Thermometers and barometers for volcanic systems. In K.D. Putirka, and F.J.
766 Tepley, Eds. *Minerals, Inclusions and Volcanic Processes*, 69, p. 61-120.
767 Mineralogical Soc Amer, Chantilly.
- 768 — (2016) Rates and styles of planetary cooling on Earth, Moon, Mars, and Vesta, using
769 new models for oxygen fugacity, ferric-ferrous ratios, olivine-liquid Fe-Mg
770 exchange, and mantle potential temperature. *American Mineralogist*, 101(3-4),
771 819-840.
- 772 Putirka, K.D., Mikaelian, H., Ryerson, F., and Shaw, H. (2003) New clinopyroxene-liquid
773 thermobarometers for mafic, evolved, and volatile-bearing lava compositions,

- 774 with applications to lavas from Tibet and the Snake River Plain, Idaho. American
775 Mineralogist, 88(10), 1542-1554.
- 776 Putirka, K.D., Perfit, M., Ryerson, F.J., and Jackson, M.G. (2007) Ambient and excess
777 mantle temperatures, olivine thermometry, and active vs. passive upwelling.
778 Chemical Geology, 241(3-4), 177-206.
- 779 Putirka, K.D., Kuntz, M.A., Unruh, D.M., and Vaid, N. (2009) Magma evolution and
780 ascent at the craters of the Moon and neighboring volcanic fields, southern Idaho,
781 USA: Implications for the evolution of polygenetic and monogenetic volcanic
782 fields. Journal of Petrology, 50(9), 1639-1665.
- 783 Putirka, K., Jean, M., Cousens, B., Sharma, R., Torrez, G., and Carlson, C. (2012)
784 Cenozoic volcanism in the Sierra Nevada and Walker Lane, California, and a new
785 model for lithosphere degradation. Geosphere, 8(2), 265-291.
- 786 Qiu, J.X. (1991) Potassium-Rich Volcanic Rocks in Wudalianchi-Keluo-Erkeshan. China
787 University of Geosciences Press, Beijing (in Chinese).
- 788 Rhodes, J.M., Dungan, M.A., Blanchard, D.P., and Long, P.E. (1979) Magma mixing at
789 mid-ocean ridges - evidence from basalts drilled near 22-degrees-N on the
790 mid-Atlantic ridge. Tectonophysics, 55(1-2), 35-61.
- 791 Richard, G.C., and Bercovici, D. (2009) Water-induced convection in the Earth's mantle
792 transition zone. Journal of Geophysical Research-Solid Earth, 114.
- 793 Richard, G.C., and Iwamori, H. (2010) Stagnant slab, wet plumes and Cenozoic
794 volcanism in East Asia. Physics of the Earth and Planetary Interiors, 183(1-2),

- 795 280-287.
- 796 Sakuyama, T., Tian, W., Kimura, J.I., Fukao, Y., Hirahara, Y., Takahashi, T., Senda, R.,
797 Chang, Q., Miyazaki, T., Obayashi, M., and others. (2013) Melting of dehydrated
798 oceanic crust from the stagnant slab and of the hydrated mantle transition zone:
799 Constraints from Cenozoic alkaline basalts in eastern China. *Chemical Geology*,
800 359, 32-48.
- 801 Shao, J., Zhang, W., Zhou, X., and Zhang, C. (2009) Discovery of Xiaogulihe perpotassic
802 basic and ultrabasic volcanic rock in the North-West Heilongjiang province,
803 China. *Acta Petrologica Sinica*, 25(10), 2642-2650 (in Chinese).
- 804 Shore, M., and Fowler, A.D. (1996) Oscillatory zoning in minerals: A common
805 phenomenon. *Canadian Mineralogist*, 34, 1111-1126.
- 806 Sobolev, S.V., Sobolev, A.V., Kuzmin, D.V., Krivolutskaya, N.A., Petrunin, A.G., Arndt,
807 N.T., Radko, V.A., and Vasiliev, Y.R. (2011) Linking mantle plumes, large igneous
808 provinces and environmental catastrophes. *Nature*, 477(7364), 312-316.
- 809 Spera, F.J. (1984) Carbon dioxide in petrogenesis III: role of volatiles in the ascent of
810 alkaline magma with special reference to xenolith-bearing mafic lavas.
811 *Contributions to Mineralogy and Petrology*, 88(3), 217-232.
- 812 Sun, Y., Ying, J.F., Zhou, X.H., Shao, J., Chu, Z.Y., and Su, B.X. (2014) Geochemistry of
813 ultrapotassic volcanic rocks in Xiaogulihe NE China: Implications for the role of
814 ancient subducted sediments. *Lithos*, 208, 53-66.
- 815 Sun, Y., Ying, J.F., Su, B.X., Zhou, X.H., and Shao, J.A. (2015) Contribution of crustal

816 materials to the mantle sources of Xiaogulihe ultrapotassic volcanic rocks,
817 Northeast China: New constraints from mineral chemistry and oxygen isotopes of
818 olivine. *Chemical Geology*, 405, 10-18.

819 Sun, Y., Teng, F.Z., Ying, J.F., Su, B.X., Hu, Y., Fan, Q.C., and Zhou, X.H. (2017)
820 Magnesium isotopic evidence for ancient subducted oceanic crust in LOMU-like
821 potassium-rich volcanic rocks. *Journal of Geophysical Research-Solid Earth*,
822 122(10), 7562-7572.

823 Takagi, D., Sato, H., and Nakagawa, M. (2005) Experimental study of a low-alkali
824 tholeiite at 1-5 kbar: optimal condition for the crystallization of high-An
825 plagioclase in hydrous arc tholeiite. *Contributions to Mineralogy and Petrology*,
826 149(5), 527-540.

827 Tamura, Y., Yuhara, M., and Ishii, T. (2000) Primary arc basalts from Daisen Volcano,
828 Japan: Equilibrium crystal fractionation versus disequilibrium fractionation during
829 supercooling. *Journal of Petrology*, 41(3), 431-448.

830 Tang, Y.J., Zhang, H.F., and Ying, J.F. (2006) Asthenosphere-lithospheric mantle
831 interaction in an extensional regime: Implication from the geochemistry of
832 Cenozoic basalts from Taihang Mountains, North China Craton. *Chemical
833 Geology*, 233(3-4), 309-327.

834 Tang, Y.C., Obayashi, M., Niu, F.L., Grand, S.P., Chen, Y.J., Kawakatsu, H., Tanaka, S.,
835 Ning, J.Y., and Ni, J.F. (2014) Changbaishan volcanism in northeast China linked
836 to subduction-induced mantle upwelling. *Nature Geoscience*, 7(6), 470-475.

- 837 Tao, K., Niu, F.L., Ning, J.Y., Chen, Y.S.J., Grand, S., Kawakatsu, H., Tanaka, S.,
838 Obayashi, M., and Ni, J. (2014) Crustal structure beneath NE China imaged by
839 NECESSArray receiver function data. *Earth and Planetary Science Letters*, 398,
840 48-57.
- 841 Tao, Y., Putirka, K., Hu, R.Z., and Li, C.S. (2015) The magma plumbing system of the
842 Emeishan large igneous province and its role in basaltic magma differentiation in
843 a continental setting. *American Mineralogist*, 100(11-12), 2509-2517.
- 844 Tian, H.C., Yang, W., Li, S.G., Ke, S., and Chu, Z.Y. (2016) Origin of low delta(26) Mg
845 basalts with EM-I component: Evidence for interaction between enriched
846 lithosphere and carbonated asthenosphere. *Geochimica et Cosmochimica Acta*,
847 188, 93-105.
- 848 Turner, M., Turner, S., Mironov, N., Portnyagin, M., and Hoernle, K. (2017) Can
849 magmatic water contents be estimated from clinopyroxene phenocrysts in some
850 lavas? A case study with implications for the origin of the Azores Islands.
851 *Chemical Geology*, 466, 436-445.
- 852 Verma, M.P. (2003) Steam tables for pure water as an ActiveX component in Visual Basic
853 6.0. *Computers & Geosciences*, 29(9), 1155-1163.
- 854 Wade, J.A., Plank, T., Hauri, E.H., Kelley, K.A., Roggensack, K., and Zimmer, M. (2008)
855 Prediction of magmatic water contents via measurement of H₂O in clinopyroxene
856 phenocrysts. *Geology*, 36(10), 799-802.
- 857 Wang, X.C., Li, Z.X., Li, X.H., Li, J., Liu, Y., Long, W.G., Zhou, J.B., and Wang, F.

- 858 (2012) Temperature, pressure, and composition of the mantle source region of late
859 Cenozoic basalts in Hainan island, SE Asia: A consequence of a young thermal
860 mantle plume close to subduction zones? *Journal of Petrology*, 53(1), 177-233.
- 861 Wang, X.C., Wilde, S.A., Li, Q.L., and Yang, Y.N. (2015) Continental flood basalts
862 derived from the hydrous mantle transition zone. *Nature Communications*, 6.
- 863 Wang, X.J., Chen, L.H., Hofmann, A.W., Mao, F.G., Liu, J.Q., Zhong, Y., Xie, L.W., and
864 Yang, Y.H. (2017) Mantle transition zone -derived EM1 component beneath NE
865 China: Geochemical evidence from Cenozoic potassic basalts. *Earth and
866 Planetary Science Letters*, 465, 16-28.
- 867 Wei, W., Hammond, J.O.S., Zhao, D.P., Xu, J.D., Liu, Q., and Gu, Y.N. (2019) Seismic
868 evidence for a mantle transition zone origin of the Wudalianchi and Halaha
869 volcanoes in Northeast China. *Geochemistry Geophysics Geosystems*, 20(1),
870 398-416.
- 871 Wilson, L. (1980) Relationships between pressure, volatile content and ejecta velocity in
872 3 types of volcanic explosion. *Journal of Volcanology and Geothermal Research*,
873 8(2-4), 297-313.
- 874 —. (2009) Volcanism in the solar system. *Nature Geoscience*, 2(6), 388-396.
- 875 Xia, Q.K., Liu, J., Liu, S.C., Kovacs, I., Feng, M., and Dang, L. (2013) High water
876 content in Mesozoic primitive basalts of the North China Craton and implications
877 on the destruction of cratonic mantle lithosphere. *Earth and Planetary Science
878 Letters*, 361, 85-97.

- 879 Xia, Q.K., Bi, Y., Li, P., Tian, W., Wei, X., and Chen, H.L. (2016) High water content in
880 primitive continental flood basalts. *Scientific Reports*, 6.
- 881 Xia, Q.K., Liu, J., Kovacs, I., Hao, Y.T., Li, P., Yang, X.Z., Chen, H., and Sheng, Y.M.
882 (2019) Water in the upper mantle and deep crust of eastern China: concentration,
883 distribution and implications. *National Science Review*, 6(1), 125-144.
- 884 Xu, Y.G., Ma, J.L., Frey, F.A., Feigenson, M.D., and Liu, J.F. (2005) Role of
885 lithosphere-asthenosphere interaction in the genesis of Quaternary alkali and
886 tholeiitic basalts from Datong, western North China Craton. *Chemical Geology*,
887 224(4), 247-271.
- 888 Xu, Z., Zhao, Z.F., and Zheng, Y.F. (2012) Slab-mantle interaction for thinning of
889 cratonic lithospheric mantle in North China: Geochemical evidence from
890 Cenozoic continental basalts in central Shandong. *Lithos*, 146, 202-217.
- 891 Zhang, M. (1984) Petrological characteristics of shihlunite of Laoheishan and
892 Huoshaoshan of Wudalianchi, Heilongjiang Province. *Earth Science - Journal of*
893 *Wuhan College of Geology*, 24, 91-142 (in Chinese).
- 894 Zhang, M., Suddaby, P., Thompson, R.N., Thirlwall, M.F., and Menzies, M.A. (1995)
895 Potassic volcanic-rocks in NE China - geochemical constraints on mantle source
896 and magma genesis. *Journal of Petrology*, 36(5), 1275-1303.
- 897 Zhang, M., Zhou, X.H., and Zhang, J.B. (1998) Nature of the lithospheric mantle beneath
898 NE China: Evidence from potassic volcanic rocks and mantle xenoliths. In M.F.J.
899 Flower, S.L. Chung, C.H. Lo, and T.Y. Lee, Eds. *Mantle Dynamics and Plate*

- 900 Interactions in East Asia, 27, p. 197-219.
- 901 Zhang, M., Suddaby, P., O'Reilly, S.Y., Norman, M., and Qiu, J.X. (2000) Nature of the
902 lithospheric mantle beneath the eastern part of the Central Asian fold belt: mantle
903 xenolith evidence. *Tectonophysics*, 328(1-2), 131-156.
- 904 Zhang, Y.L., Liu, C.Z., Ge, W.C., Wu, F.Y., and Chu, Z.Y. (2011) Ancient sub-continental
905 lithospheric mantle (SCLM) beneath the eastern part of the Central Asian
906 Orogenic Belt (CAOB): Implications for crust-mantle decoupling. *Lithos*,
907 126(3-4), 233-247.
- 908 Zhao, D.P., Tian, Y., Lei, J.S., Liu, L.C., and Zheng, S.H. (2009) Seismic image and
909 origin of the Changbai intraplate volcano in East Asia: Role of big mantle wedge
910 above the stagnant Pacific slab. *Physics of the Earth and Planetary Interiors*,
911 173(3-4), 197-206.
- 912 Zhao, D.P., Yu, S., and Ohtani, E. (2011) East Asia: Seismotectonics, magmatism and
913 mantle dynamics. *Journal of Asian Earth Sciences*, 40(3), 689-709.
- 914 Zhao, Y.W., Fan, Q.C., Zou, H.B., and Li, N. (2014a) Geochemistry of Quaternary
915 basaltic lavas from the Nuomin volcanic field, Inner Mongolia: Implications for
916 the origin of potassic volcanic rocks in Northeastern China. *Lithos*, 196, 169-180.
- 917 Zhao, Y.W., Li, N., Fan, Q.C., Zou, H.B., and Xu, Y.G. (2014b) Two episodes of
918 volcanism in the Wudalianchi volcanic belt, NE China: Evidence for tectonic
919 controls on volcanic activities. *Journal of Volcanology and Geothermal Research*,
920 285, 170-179.

921 Zhao, Y., Zhang, Y.G., Geng, M., Jiang, J.L., and Zou, X.Y. (2019) Involvement of
922 slab-derived fluid in the generation of Cenozoic basalts in Northeast China
923 inferred from machine learning. *Geophysical Research Letters*, 46(10),
924 5234-5242.

925 Zheng, Y., Shen, W.S., Zhou, L.Q., Yang, Y.J., Xie, Z.J., and Ritzwoller, M.H. (2011)
926 Crust and uppermost mantle beneath the North China Craton, northeastern China,
927 and the Sea of Japan from ambient noise tomography. *Journal of Geophysical*
928 *Research-Solid Earth*, 116.

929 Zhou, X.H., Zhu, B.Q., Liu, R.X., and Chen, W.J. (1988) Cenozoic basaltic rocks in
930 Eastern China. In J.D. Macdougall, Ed. *Continental Flood Basalts*, p. 311-330.
931 Springer Netherlands, Dordrecht.

932 Zou, H.B., Reid, M.R., Liu, Y.S., Yao, Y.P., Xu, X.S., and Fan, Q.C. (2003) Constraints on
933 the origin of historic potassic basalts from northeast China by U-Th
934 disequilibrium data. *Chemical Geology*, 200(1-2), 189-201.

935

936

Figure captions

937 **Figure 1.** Schematic map of the late Cenozoic intraplate volcanic province in
938 Central-East Asia, modified after Wang et al. (2015). The dark gray fields and numbers
939 indicate the locations of the late Cenozoic volcanic fields in Central–East Asia. The thick
940 solid white curves represent plate boundaries. The red dashed curve indicates the western
941 edge of the present-day stagnant Pacific slab (Zhao et al. 2011). Digital topography of

942 Central-East Asia is from National Oceanic and Atmospheric Administration/National
943 Geophysical Data Center (<http://www.ngdc.noaa.gov/mgg/image/>).

944

945 **Figure 2.** Representative photographs of the WEK basalt samples. **(a)** Back-scattered
946 electron (BSE) image of a euhedral, zoned clinopyroxene phenocryst from sample HSS5.
947 **(b)** Microphotograph of sample HSS5, showing glassy features. Clinopyroxene
948 phenocrysts are distributed in the groundmass, which is composed of glass with
949 subordinate clinopyroxene, olivine, and K-feldspar microcrystals. Note the substantial
950 bubbles present in the rock. Cpx denotes clinopyroxene. **(c)** Field photograph of a surface
951 lava flow of Laoheishan volcano, showing rope-like features, a volcanic bomb, and
952 elongated bubbles. **(d)** Microphotograph of sample HSS8 showing a euhedral olivine
953 crystal with embayment structure. Ol denotes olivine.

954

955 **Figure 3.** Tests for the thermobarometers. **(a)** Rhodes' diagram (Rhodes et al. 1979) for
956 clinopyroxene in the WEK potassic basalts. $Mg\# = 100 \times Mg / (Mg + Fe^{2+})$, where Mg and
957 Fe^{2+} are in molar fraction. Here the proportion of Fe^{2+} is set to be 100%, following the
958 treatment in experimental calibration (Putirka, 2008). Solid curve: the mean value of the
959 experimental $K_D(Fe-Mg)^{cpx-melt}$; two dashed curves: 2σ range of the mean experimental
960 $K_D(Fe-Mg)^{cpx-melt}$; grey field: the range of all experimental $K_D(Fe-Mg)^{cpx-melt}$ (Putirka
961 2008). **(b)** Mg# of clinopyroxene vs. crystallization pressure (P) calculated using the
962 clinopyroxene–melt barometer of Putirka et al. (2003). The Mg# value of clinopyroxene

963 has a normal distribution and yields an average of 81.9 ± 4.8 (2σ), without a decreasing
964 trend as the crystallization pressure decreases. (c) Measured vs. predicted clinopyroxene
965 composition using equations (3.1a), (3.2) and (3.5) of [Putirka \(1999\)](#). All the
966 clinopyroxene grains in equilibrium with their melts are plotted on the 1:1 line within
967 prediction error. DiHd denotes the diopside–hedenbergite component in pyroxene; EnFs
968 denotes the enstatite–ferrosilite component in pyroxene; Jd denotes the jadeite component
969 in pyroxene. (d) Comparison of pressure (P) estimates using the [Lee et al. \(2009\)](#) and
970 [Putirka \(2008\)](#) Si activity barometers for the WEK basalts. Input temperatures are the
971 same in both barometers, which are calculated using the [Lee et al. \(2009\)](#) thermometer
972 with a melt H_2O content of 4.5 wt%. The two barometers yield identical pressure
973 estimates within error.

974

975 **Figure 4. (a)** Pressure–temperature calculation results of the clinopyroxene–melt
976 thermobarometer ([Putirka et al. 2003](#)) and the Si activity thermobarometer ([Lee et al.](#)
977 [2009](#)) for the WEK basalts. The results of the clinopyroxene–melt thermobarometer (blue
978 circles and the blue field) are linearly fitted and yield $dT/dP = 8.8$ °C/kbar. The Si activity
979 pressures and temperatures are calculated based on different H_2O concentration estimates,
980 which are 0.50 wt% ([Chen et al. 2015](#); red field), 1.4 wt% ([Kuritani et al. 2013](#); green
981 field) and 4.5 wt% (our best estimation value; gray field). Error bars and ellipses are
982 drawn according to [Putirka et al. \(2003\)](#) and [Lee et al. \(2009\)](#). Buffers are constructed for
983 the clinopyroxene–melt thermobarometer and the Si activity thermobarometer by

984 outlining the corresponding P – T points with their error ellipses; see the text for details.
985 Black dashed curves represent clinopyroxene saturation surfaces of the HSS5 melt with
986 H₂O contents of 4 and 5 wt%, calculated using the equation (34) of [Putirka \(2008\)](#). **(b)**
987 Relationship between the buffer overlapping area/maximal buffer overlapping area
988 (BOA/BOAmax) ratio and the melt H₂O content used in the Si activity thermobarometer
989 calculation. The upright dashed line shows the best estimation of the melt H₂O content,
990 which is 4.5 wt%.

991

992 **Figure 5.** Estimated vs. experimental **(a)** melt H₂O content, **(b)** pressure, and **(c)**
993 temperature, using the experimental data listed in [Table 2](#). Melt H₂O contents are
994 estimated using the same method as used for the WEK basalts. Pressures and
995 temperatures are calculated using the Si activity thermobarometer ([Lee et al. 2009](#)) with
996 the estimated H₂O contents in **(a)**. Red lines show linear fittings of the data points. SEE
997 (standard estimate error) = $\sqrt{\sum(X_{\text{est}} - X_{\text{true}})^2/N}$, where X_{est} is the estimated value, X_{true}
998 is the true value, N is the number of data.

999

1000 **Figure 6.** Modeled H₂O–CO₂ degassing curves of the WEK magma. Degassing curves
1001 are calculated using the model of [Duan \(2014\)](#) and the HSS5 melt composition. The
1002 initial state is H₂O = 4.5 wt% and CO₂ = 2.0 wt% at 13.5 kbar and 1438 K. The red and
1003 black curves represent degassing in closed and open system, respectively. The gray
1004 curves are H₂O–CO₂ solubility isobars. The temperature of each isobar is the same as that

1005 of the magma, i.e., determined by $P/\text{kbar} = -118.0 + 0.113 T/^\circ\text{C}$. The blue curves are
1006 curves of identical vapor composition. The numbers on these curves represent the molar
1007 fraction of H_2O in the vapor phase.

1008

1009 **Figure 7. (a)** P - T path of the WEK magmas extending to higher pressures. Compositions
1010 of the low- SiO_2 samples are from [Zhang et al. \(1995\)](#) (DZ-6, DZ-3, H-1, MH-4, A-2,
1011 H-38); other data points are the same as in [Fig. 4a](#). Silica activity pressures and
1012 temperatures are calculated using the estimated 4.5 wt% melt H_2O content. Dry and wet
1013 ($X_{\text{H}_2\text{O}}^{\text{bulk}} = 450$ ppm) peridotite solidi are plotted using the parameterization of [Katz et al.](#)
1014 [\(2003\)](#). Mantle potential temperature (T_p) is calculated using the model of [Putirka \(2016\)](#),
1015 with composition and pressure inputs from the most primary WEK samples. **(b)**
1016 Schematic illustration of the origin of the WEK magmas. Hydrated mantle materials
1017 originating from the mantle transition zone (MTZ) crossed the solidus during their
1018 upwelling in the convective mantle, and generated small-degree partial melts. The melts
1019 stalled at the base of the lithosphere, followed by extraction and rapid magma ascent to
1020 the surface. The local Moho depth of 31.3 ± 0.6 km is from [Tao et al. \(2014\)](#); the
1021 lithosphere–asthenosphere boundary (LAB) depth of 70–80 km is from [Zheng et al.](#)
1022 [\(2011\)](#), [Li et al. \(2012, 2013\)](#), and [Guo et al. \(2014\)](#). Depth and pressure are translated
1023 assuming a crust average density of 2.7 g/cm^3 and a lithospheric mantle average density
1024 of 3.3 g/cm^3 , following [Tao et al. \(2014\)](#).

1025

1026 **Figure 8.** Pressure–H₂O content relation of the Xiaogulihe melts recorded by
1027 clinopyroxene crystals. Pressures are calculated using the [Putirka et al. \(2003\)](#)
1028 thermobarometer with clinopyroxene and bulk-rock compositions from [Chen et al. \(2015\)](#).
1029 Only the clinopyroxene crystals with $K_D(\text{Fe–Mg})^{\text{cpx–melt}}$ between 0.12 and 0.44 were used
1030 for P estimation. The melt H₂O contents corresponding to the clinopyroxene phenocrysts
1031 are from [Chen et al. \(2015\)](#).

1032 **Table 1.** Example temperature differences at similar pressures calculated using the two
 1033 thermobarometers.

H ₂ O (wt%)	Overlapping pressure (kbar)	<i>P</i> (cpx–melt) ^a (kbar)	<i>T</i> (cpx–melt) ^a (°C)	<i>P</i> (Si activity) ^b (kbar)	<i>T</i> (Si activity) ^b (°C)	Δ <i>T</i>] ^c (°C)
0	8.6–13.5	8.8	1120	8.8	1164	44
		9.1	1121	9.0	1163	42
		9.6	1127	9.6	1171	44
		10.2	1131	10.2	1175	44
		11.3	1140	11.4	1207	67
0.5	8.8–13.5	8.8	1120	8.8	1170	50
		9.5	1125	9.5	1166	41
		10.3	1134	10.3	1182	48
		10.6	1137	10.6	1184	47
		11.6	1140	11.6	1201	61
1.4	9.1–13.5	9.1	1151	9.1	1121	30
		9.3	1104	9.3	1124	20
		10.0	1129	10.0	1159	30
		10.8	1135	10.8	1175	40
		11.8	1192	11.9	1146	46
3	9.6–13.5	9.6	1127	9.6	1139	12
		10.0	1141	10.0	1129	12
		10.5	1147	10.5	1135	12
		11.3	1161	11.3	1140	21
		12.3	1176	12.3	1149	27
5	10.3–13.5	10.3	1134	10.3	1134	0
		10.6	1137	10.6	1128	9
		11.0	1137	11.0	1132	5
		11.9	1146	11.9	1145	1
		12.8	1154	12.8	1158	4
7	10.9–13.5	10.9	1136	10.9	1114	22
		11.3	1140	11.2	1116	24
		11.6	1140	11.6	1120	20
		12.4	1149	12.4	1125	24
		13.5	1162	13.3	1143	19
9	11.5–13.5	11.6	1140	11.5	1105	35
		11.9	1146	11.9	1107	39
		12.3	1149	12.2	1110	39
		12.4	1149	12.4	1111	38

12.7

1154

12.8

1119

35

1034 ^a Pressures and temperatures are calculated using the clinopyroxene–melt
1035 thermobarometer of [Putirka et al. \(2003\)](#).

1036 ^b Pressures and temperatures are calculated using the Si activity thermobarometer of [Lee](#)
1037 [et al. \(2009\)](#).

1038 ^c $|\Delta T| = |T(\text{cpx–melt}) - T(\text{Si activity})|$. Note $|\Delta T|$ is minimized at H₂O content of 5 wt%.

1039

1040

1041 **Table 2.** Summary of the experimental data used for testing the water content estimation method.

LEPR Index	Reference	<i>P</i> (kbar)	<i>T</i> (°C)	Phases ^a	H ₂ O ^{melt} (wt%)	H ₂ O ^{melt} error ^b (wt%)	Estimated H ₂ O ^c (wt%)	Estimated <i>P</i> ^d (kbar)	Estimated <i>T</i> ^d (°C)
2269	Müntener et al. (2001)	12	1230	liq+ol+cpx+opx	5.80	0.02	4.4	9.2	1175
2440	Hesse and Grove (2003)	16	1380	liq+ol+opx+cpx	2.8	n.r.	1.3	14.8	1280
3227	Takagi et al. (2005)	2	1030	liq+ol+plag+cpx+opx+spn	4.5	n.r.	3.4	-0.4	1082
4573	Gaetani and Grove (1998)	12	1245	liq+cpx+opx+ol+spn	3.3	0.3	3.8	14.3	1263
4575	Gaetani and Grove (1998)	12	1215	liq+cpx+opx+ol+spn	5.99	0.05	4.6	14.6	1241
4576	Gaetani and Grove (1998)	12	1200	liq+cpx+opx+ol+spn	5.06	0.04	4.9	13.3	1223
4577	Gaetani and Grove (1998)	12	1185	liq+cpx+opx+ol+spn	6.3	0.1	5.0	12.6	1207
4583	Gaetani and Grove (1998)	16	1260	liq+cpx+opx+ol+spn+gt	4.9	1.1	4.7	17.5	1268
4584	Gaetani and Grove (1998)	16	1255	liq+cpx+opx+ol+spn+gt	5.0	0.6	4.9	17.3	1267
4585	Gaetani and Grove (1998)	16	1245	liq+cpx+opx+ol+spn	5.3	0.5	4.8	17.4	1267

4586	Gaetani and Grove (1998)	16	1230	liq+cpx+opx+ol+gt	4.8	0.6	5.4	16.4	1245
4589	Gaetani and Grove (1998)	20	1290	liq+cpx+opx+ol+gt	5.3	0.6	5.7	19.6	1280
4590	Gaetani and Grove (1998)	20	1275	liq+cpx+opx+ol+gt	6.8	0.4	4.6	18.6	1290
4595	Gaetani and Grove (1998)	12	1185	liq+cpx+opx+ol+spn	6.2	0.4	5.0	13.5	1196
5063	Kelemen et al. (1990)	4.985	1052	liq+ol+cpx+opx+amph+ilm	4.3	0.4	5.4	7.7	1134
20068	Grove et al. (2013)	22	1410	liq+cpx+opx+ol+spn	3.0	0.2	1.0	21.6	1352
20074	Grove et al. (2013)	24	1410	liq+cpx+opx+ol+gt	2.95	0.25	3.5	23.6	1294
55001	Gaetani et al. (2003)	12	1315	liq+cpx+opx+ol+spn	0.98	0.24	3.0	14.8	1275
55002	Gaetani et al. (2003)	12	1185	liq+cpx+opx+ol+spn	6.3	0.1	5.0	12.6	1207
55003	Gaetani et al. (2003)	16	1370	liq+cpx+opx+ol+spn	1.70	0.17	2.1	17.4	1333
55004	Gaetani et al. (2003)	16	1230	liq+cpx+opx+ol+gt	4.8	0.6	5.4	16.4	1245

1042 ^a liq = liquid, ol = olivine, cpx = clinopyroxene, opx = orthopyroxene, plag = plagioclase, spn = spinel, grt = garnet, amph =

1043 amphibole, ilm = ilmenite.

1044 ^b n.r., not reported.

1045 ^c H₂O content when BOA is maximized.

1046 ^d Pressures and temperatures are calculated using the Si activity thermobarometer (Lee et al. 2009) with the estimated melt H₂O
1047 contents.

1048

1049

1050 **Table 3.** Thermal expansion coefficient (α), specific heat capacity (c_p), and density (ρ)
1051 data of basaltic melts, water, and carbon dioxide at 1400 K and 10 kbar.

	α (10^{-4} K^{-1})	c_p [$10^3 \text{ J}/(\text{kg}\cdot\text{K})$]	ρ ($10^3 \text{ kg}/\text{m}^3$)	$(\partial T/\partial P)_S^e$ ($^\circ\text{C}/\text{kbar}$)
Volatile-free HSS5 melt ^a	0.72	1.4	2.8	2.5
Basaltic melt ^b	0.68	1.0	2.8	3.4
H ₂ O ^c	4.1	3.4	0.8	22
CO ₂ ^d	3.2	1.5	1.1	28

1052 ^a Calculated using the partial molar thermodynamic properties from [Leshner and Spera](#)
1053 [\(2015\)](#); the melt composition is from [Chu et al. \(2013\)](#).

1054 ^b From [McKenzie and Bickle \(1988\)](#).

1055 ^c Calculated using the model of [Verma \(2003\)](#).

1056 ^d From [Bottinga and Richet \(1981\)](#).

1057 ^e $(\partial T/\partial P)_S = T\alpha/(\rho c_p)$, where T is the temperature (1400 K).

Figure 1

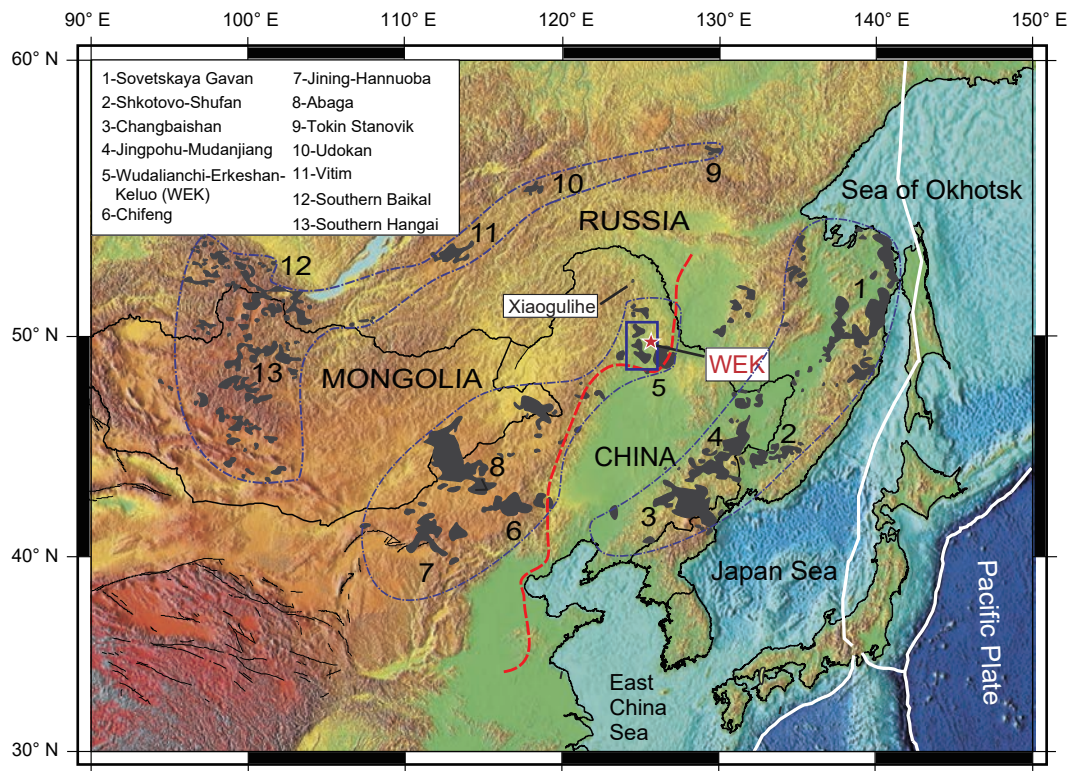


Figure 2

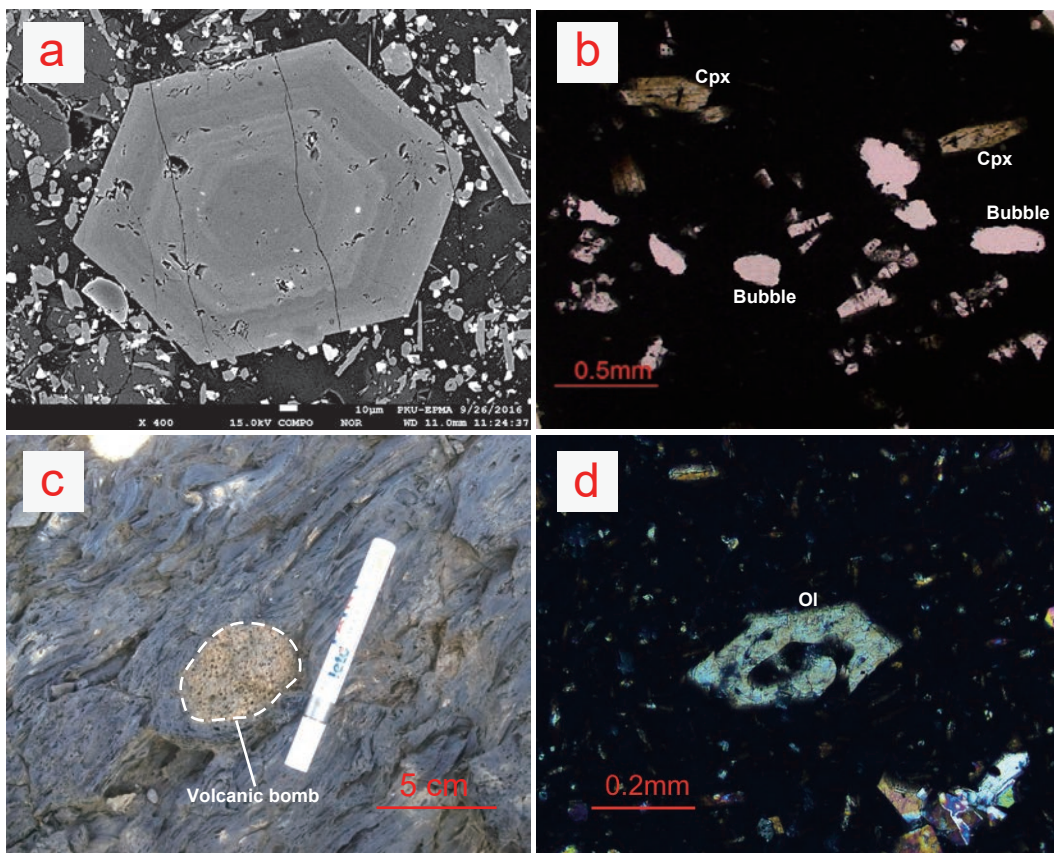


Figure 3

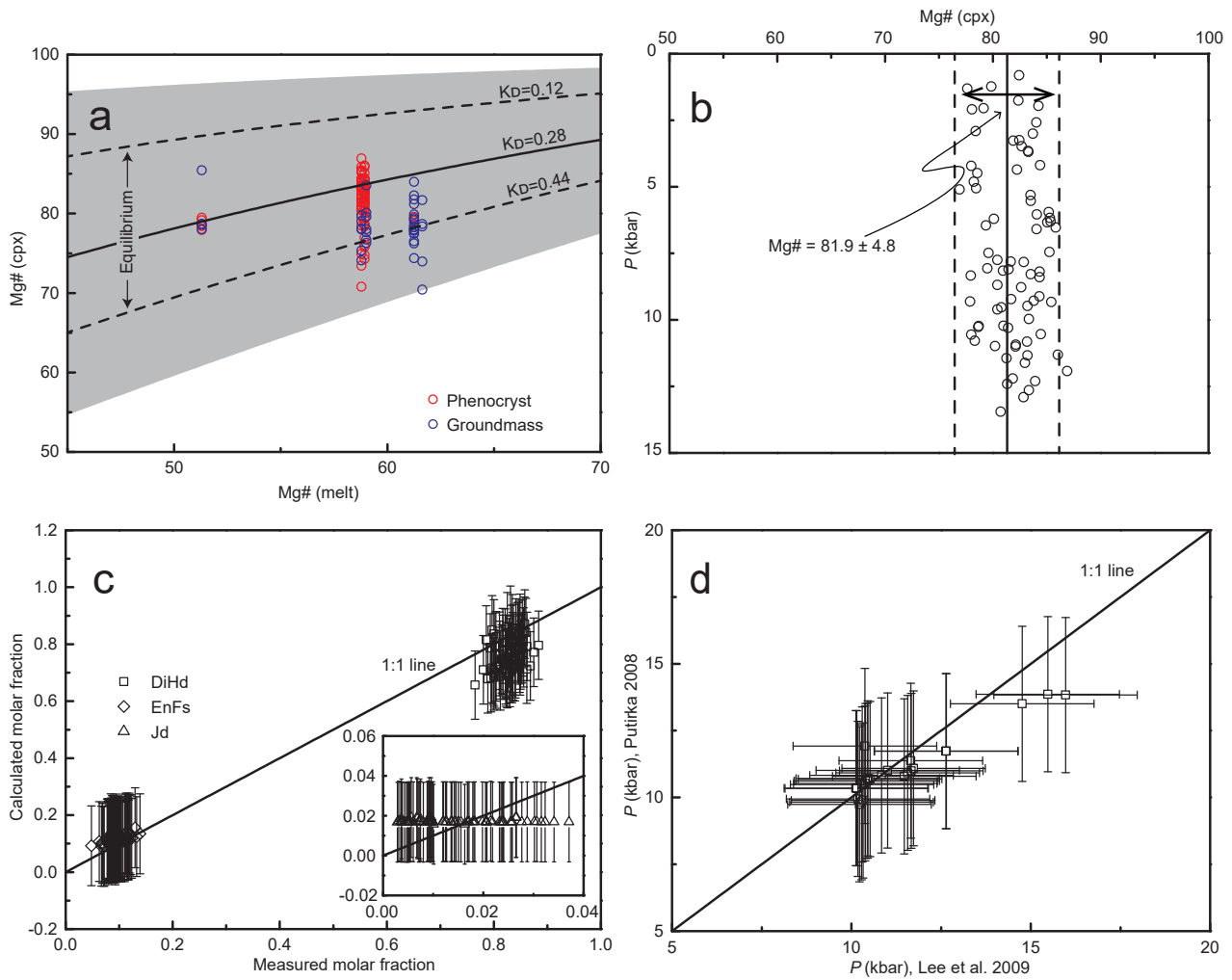


Figure 4

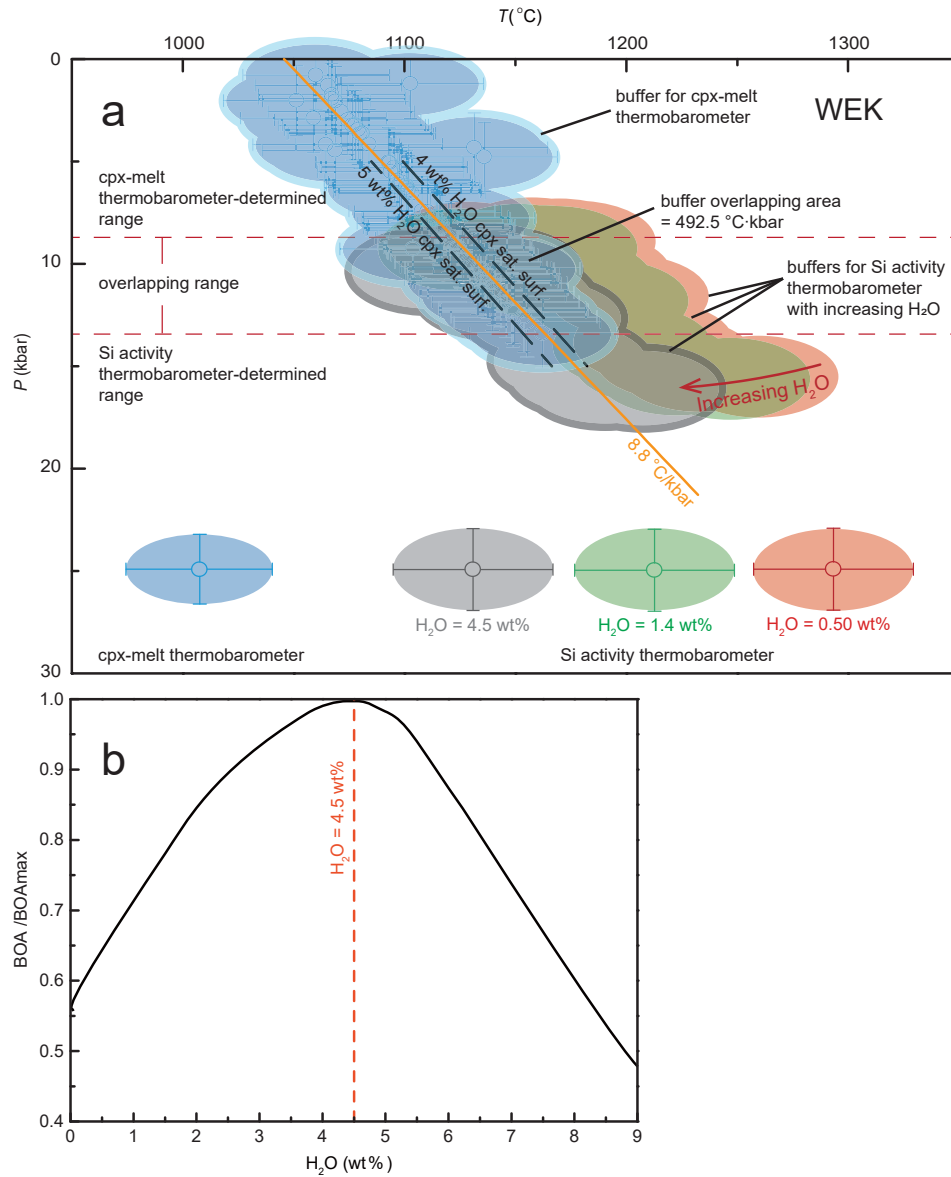


Figure 5

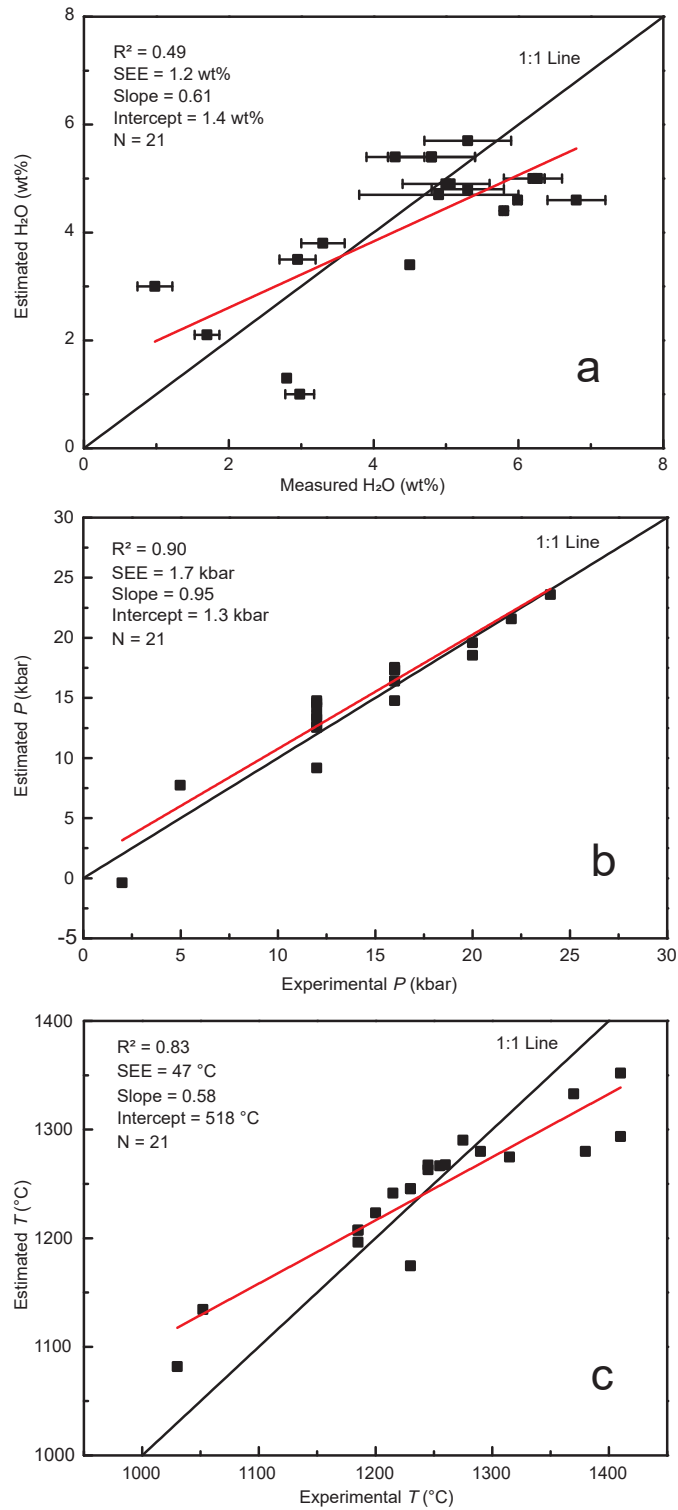


Figure 6

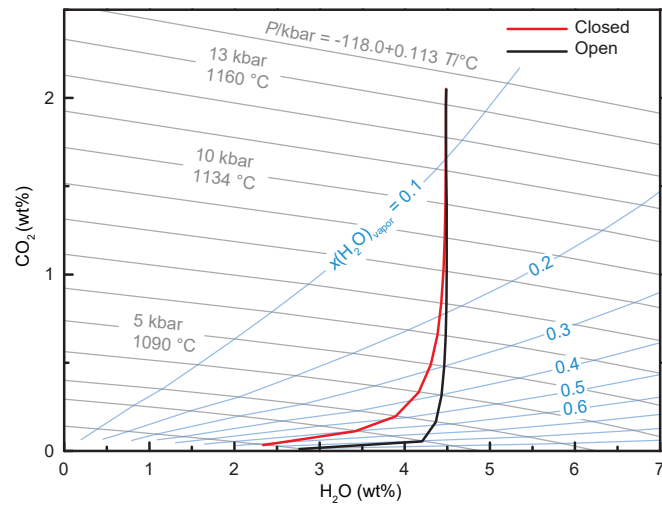


Figure 7

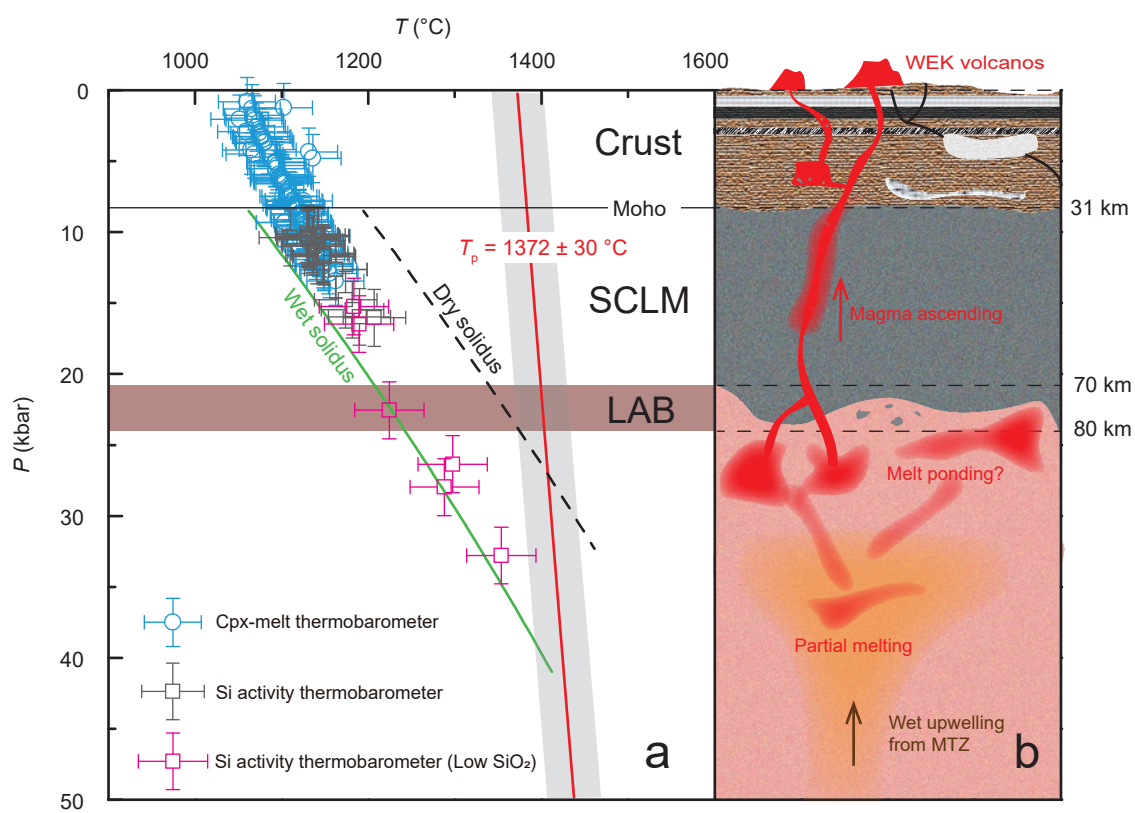


Figure 8

